An urban large-eddy simulation-based dispersion model for marginal grid resolutions: CAIRDIO v1.0

Michael Weger[1], Oswald Knoth[1], and Bernd Heinold[1]

[1]Leibniz Institute for Tropospheric Research, Leipzig, Germany

Correspondence: Michael Weger (weger@tropos.de)

Abstract. The ~~capability for~~ ability to achieve high spatial resolutions is an important feature of ~~accurate numerical models dedicated to simulate~~ numerical models to accurately represent the large spatial variability of urban air pollution. On the one hand, the well established mesoscale chemistry transport models have their obvious short-comings ~~attributed to their~~ due to the extensive use of parameterizations. On the other hand, obstacle resolving computational fluid dynamic models CFD, ~~while~~ although accurate, ~~still often demand too high computational costs~~ are still often too computationally intensive to be applied ~~on a regular basis~~ regularly for entire cities. The major reason for the inflated ~~numerical~~ computational costs is the required horizontal resolution to meaningfully apply ~~the~~ obstacle discretization, which is most often based on boundary-fitted grids, like e.g. the marker-and-cell method. ~~Here we present a large-eddy-simulation approach that uses diffusive obstacle boundaries, which are derived from a simplified diffusive interface approach for moving obstacles.~~ In this paper, we present the new City-scale AIR dispersion model with DIffuse Obstacles (CAIRDIO v1.0), in which the diffuse interface method, simplified for non-moving obstacles, is incorporated into the governing equations for incompressible large-eddy simulations. While ~~T~~the diffusive interface approach is ~~well established~~ widely used in two-phase modeling, ~~but to the author's knowledge~~ this method has not been ~~applied~~ used in urban boundary layer ~~simulations~~ modeling so far. ~~Our dispersion model is capable of representing~~ It allows to consistently represent buildings over a wide range of spatial resolutions, including grid spacings equal or larger than typical building sizes. ~~This opens up a very promising opportunity for application of accurate air quality simulations and forecasts on entire mid-sized city domains.~~ This way, the gray-zone between obstacle-resolving microscale simulations and mesoscale simulations can be addressed. ~~Furthermore, our approach is capable of incorporating the influence of the land orography by the additional optional use of terrain-following coordinates.~~ Orographic effects can be included by using terrain-following coordinates. ~~We validated t~~The dynamic core is compared against a ~~set of numerical benchmarks and a~~ standard ~~high-~~quality-assured wind-tunnel data~~-~~set for dispersion-model evaluation. It is shown that the model successfully reproduces dispersion patterns within a complex city morphology across a wide range of spatial resolutions tested. As a result of the diffuse obstacle approach, the accuracy test is also passed at a horizontal grid spacing of 40 m. Although individual flow features within individual street canyons are not resolved at the coarse grid spacing, the building effect on the dispersion of the air pollution plume is preserved at a larger scale. Therefore, a very promising application of the CAIRDIO model lies in the realization of computationally feasible yet accurate air quality simulations for entire cities.

1 Introduction

The state-of-the-art in urban air quality modeling now almost routinely ~~incorporates~~ encompasses the scales at which processes governing the atmospheric dispersion inside the urban planetary boundary layer (PBL) are explicitly represented (Benavides et al., 2019; Croitoru and Nastase, 2018; Kadaverugu et al., 2019). The reasons for this increase in physical detail are manifold. On the one hand, even ~~if~~ though PBL mixing processes ~~can be~~ are often parameterized to a large extend, the parameterizations ~~itself~~ themselves must rely on a sound physical basis, for which often detailed large-eddy simulations (LES) ~~are~~ can be consulted (Noh and Raasch, 2003; Kanda et al., 2013). ~~A d~~Direct benefits of more detailed numerical simulations ~~is the~~ include an increased ability to ~~provide~~ produce more representative air-quality forecasts for individual locations (Carlino et al., 2016) and the provision of high-resolution ~~urban air-quality~~ 4-dimensional data for research purposes, like, e.g., ~~studying~~ source attribution (Fernández et al., 2019)~~,~~ and exposure risk assessment (Chang, 2016).~~, and eventually to provide more representative forecasts for individual locations (Carlino et al., 2016).~~ Exposure-relevant ~~pedestrian-level~~ air pollution concentrations at pedestrian level are subjected to a considerable and also complex spatio-temporal variability, as they are not only influenced by the relative location of pollution sources, but also very importantly by the urban morphology and ~~the interacting~~ associated meteorological conditions (Birmili et al., 2013; Paas et al., 2016; Harrison, 2018). For an accurate simulation, it is thus not only key to explicitly represent the urban canopy features, but also to consider the ~~mesoscale~~ prevailing mesoscale meteorological conditions~~ surrounding cities~~. Depending on the level of physical detail, a trade-off in the use of high-resolution numerical simulations is often ~~remains~~ their exclusive ~~limited-area~~ applicability in a limited area, which can be very restrictive. ~~As a result~~ Hence, an active topic of research is dedicated to ~~the increase in~~ improve the numerical efficiency of high-resolution modeling tools and their incorporation into a larger modeling framework (Baik et al., 2009; Jensen et al., 2017; Kurppa et al., 2020).

Commonly used multiscale approaches consist of nested domains and involve different types of models designed for a specific scale range. To address the global and regional scales, the use of chemistry transport models (CTM) in combination with numerical weather prediction (NWP) models is a well established practise. Examples of ~~such model combinations~~ those coupled model systems include, C-IFS (Flemming et al., 2015), WRF-Chem (Grell et al., 2005), CMAQ (Appel et al., 2017), ICON-ART (Rieger et al., 2015) and COSMO-MUSCAT (Wolke et al., 2004, 2012). In all of these models, subgrid-scale effects of temperature and moisture, as well as PBL dynamics are parameterized. The influence of the urban canopy on the PBL in NWP models can be considered through sophisticated canopy parameterizations (Martilli et al., 2002; Schubert et al., 2012). The improvements of these so-called urbanized NWP~~'~~s are substantially reflected in modeled pollutant concentrations (Kim et al., 2015; Wang et al., 2019). Nevertheless, as the model domain ~~contains~~ does not allow for an ~~no~~ explicit representation of buildings, the pollutants emitted at street level are diluted ~~throughout~~ over the entire grid cell, which can considerably deviate from real conditions, where a large part of the physical volume may be ~~inaccessible~~ impervious. As a result, pollutant concentrations modeled using NWP-based approaches are more representative to the urban back~~-~~ground (Korhonen et al., 2019). Another practical ~~resolution and hitherto accuracy~~ limit to resolution and accuracy of NWP models ~~results~~ arises from the use of parameterizations ~~itself~~ themselves. Using WRF, Haupt et al. (2019) observed that for horizontal grid spacings below the typical ~~height of the~~ PBL height, numerical results can become spurious. Based on their findings, they recommend not to apply NWPs on the sub-kilometer scale without careful replacement of the used parameterizations. In PBL meteorology, the microscale seamlessly follows seamless at the lower limit of the mesoscale (super-kilometer range) (Stull, 1988; Rakai and Gergely, 2013). However, adopting the modeling perspective, there is a clear segregation of ~~the~~ micro~~scale from the~~ and mesoscale. While the latter is ~~truncated~~ constrained at the lower end of the resolution ~~end through~~ by the extensive use of parameterizations, ~~the~~ attempting to model urban PBL processes directly ~~using~~ with microscale approaches requires ~~an adequate spatial resolution (few tens of meters)~~ sufficiently fine grid spacings. The landscape of microscale models is diverse (Fallah-Shorshani et al., 2017; Brown, 2014; Hanna et al., 2006) and it reflects the difficulty ~~in trading off~~ of finding a compromise between computational resources and accuracy. Computational fluid dynamics models (CFD) can be seen as the microscale pedants to ~~The microscale pendants of~~ NWPs. ~~can be considered as the computational fluid dynamics (CFD) models, a~~Among them, LES approaches are the most accurate but expensive ones. LES models resolve the turbulent spectra up to the filter cut-off size (often equivalent to the the grid size) and rely on simplistic sub-scale parameterizations only (e.g. Maronga et al., 2019). These two different approaches (extensive parameterization vs. explicit representation) are difficult to merge at the bridging scale-range (few tens of meters to one kilometer), for which reason Haupt et al. (2019) ~~introduced~~ coined the key word "terra-incognita" to refer to the problem. An exemplary study, ~~where~~ in which a LES model was applied for ~~have been attempted at~~ horizontal resolutions up to above $100\,\mathrm{m}$, is given by Efstathiou et al. (2016). However, their simulations did not include an urban canopy, whose discretization would ~~impose a much stringend resolution limit~~ obviously require a much finer grid. ~~In fact, obstacle-resolving urban LES (ULES) studies are typically performed at spatial resolutions of less than 10 m to 20 m. Even at such comparatively coarse resolutions, computational resources are still the limiting factor as they restrict ULES applications to research purposes or to areas encompassing city parts only (Wolf et al., 2020). Further depending on the degree of physical detail (e.g. costly radiative transfer calculations in a complex urban environment), ULES have not yet become feasible choices to simulate air-quality in cities on a regular basis, despite their obvious advantages concerning physical accuracy.~~ In fact, to fully resolve the energy-dominant eddies within street-canyons, a spatial resolution of 15-20 grid points over a typical obstacle dimension size is needed (Xie and Castro, 2006). This translates in a grid spacing of about $1\,\mathrm{m}$ for typically sized buildings. The use of such fine grids for entire city domains is still prohibitively expensive in LES modeling. E.g., Wolf et al. 2020 used a grid spacing of $10\,\mathrm{m}$ in their cutting-edge research study to simulate air pollutant dispersion in Bergen, Norway with the LES-model PALM. While this spatial resolution, according to the argument above, does not ensure a LES model to be eddy resolving in every part of the domain, the preference of a physically-based model over the more widely used parameterized models for this grid size (e.g. plume or street-canyon models) can nevertheless be a legitimate choice. Resolved physics can still be maintained outside the densely built urban canopy. Within the canopy, the dispersion pattern on a larger scale is mostly shaped by the channeling and blocking effects of buildings, which can be represented also with coarser grids.

In physical computing, it is well known that only a slight increase in the grid spacing results in a large computational saving (e.g. models using explicit time integration ~~are~~ ideally ~~integrated~~ perform 16 times faster on the same domain using a grid with doubled grid spacings in all 3 dimensions). ~~The~~ These computational savings could in turn ~~could~~ be ~~invested~~ spent in larger physical domains for more ~~holistic~~ comprehensive yet accurate urban air-quality simulations. ~~The additional domain extend~~

~~would also provide an additional relaxation fetch for the mesoscale forcing in case complete cities are attempted to be modeled. As a result of an increased grid spacing, the level of detail of modeled wind fields clearly decreases. Nevertheless, the effect of a lower spatial resolution on the accuracy of dispersion simulations can be expected to be less detrimental in practical modeling examples, as it is affected also by other major uncertainties, like e.g. emission distribution.~~

~~The~~ A key feature ~~which~~ that sets the technical limit to the ~~model~~ spatial resolution ~~of ULES applications~~ in urban boundary-layer modeling is ~~clearly~~ the ~~spatial~~ discretization method used ~~of~~ for obstacles. A class of methods ~~in which~~ that allow for ~~the~~ obstacle geometr~~y~~ies ~~is~~ not ~~tied~~ bound to the grid are the immersed boundary methods, summarized by Mittal and Iaccarino (2005). These are essentially Cartesian methods, but instead of relying on a commonly used marker-and-cell method (grid cells are assigned either to the building interiors or to the atmosphere), they ~~aim at~~ represent~~ing~~ rigid ~~the~~ boundary conditions ~~associated with a rigid boundary~~ (e.g. Neumann boundary condition for pressure) on grid cell faces not coinciding with the obstacle boundary. Among these methods, the so-called direct forcing uses the ghost-cell interpolation technique, where image points from adjacent interior ghost points are mirrored across the rigid boundary and interpolated using surrounding fluid nodes. While this method greatly enhances the flexibility in the choice of the grid size, it still suffers from the empirical nature in the selection of the interpolation nodes and the interpolation method itself. On the other hand, an equivalent boundary forcing can be more rigorously deduced from a two-phase flow model (Drew, 1983) ~~when~~ by neglecting the restoring source terms. Treating ~~the second phase~~ one of the phases as an indeformable solid, Kemm et al. (2020) derived a ~~diffusive~~ diffuse interface (DI) model for compressible fluids. One of the main advantages of their approach is the algorithmic simplicity, as the boundary-forcing term is analytically coupled to the DI, which is advected as a scalar.

In this work, we ~~represent a new LES-based dispersion model as~~ adopt the basic idea of DI and implement diffuse obstacle boundaries (DOB) in our new City-scale AIR dispersion model with DIffuse Obstacles (CAIRDIO v1.0), which will be used as a computationally feasible yet accurate downscaling tool for mesoscale ~~meteorology and~~ air pollution fields over urban areas. ~~The development adopts the basic idea of DI, as it is simple and efficient to implement and provides a high~~ DOB allow buildings to be represented as diffuse features, and thus the flexibility in the choice of ~~the spatial~~ grid resolution can be greatly increased. ~~As the city-structure is assumed to be static, DI simplifies to static diffusive obstacle boundaries (DOB).~~ DOB is a simplified form of DI resulting from the static boundaries associated with buildings. ~~By considering the conservation law in a finite-volume framework, DOB is incorporated in the discrete differential operators, making the governing equations appear in their familiar form.~~ DOB is incorporated in the discrete differential operators by considering the conservation laws in a finite volume framework. The ~~LES~~ equations ~~can~~ are then ~~be~~ solved ~~on a structured Cartesian grid~~ with standard methods on a Cartesian grid. To interpret our DOB approach from a physical point of view, it can be argued that the grid cells are interspersed with a porous and semi-permeable medium~~., whose~~ Their detailed structure is only of concern insofar as ~~to which degree it modifies~~ it determines the mass and momentum budged at the grid level through two different types of interface fields. To the authors knowledge, this approach has not been used for air quality modeling so far, but very interestingly the concept of permeability finds application in geological science (Haga, 2011). In contrast to geometry-aligned discretizations, which preserve a high degree of accuracy near obstacle walls but require high resolutions, this approach suits more to the integral aspect of building shapes and configurations at marginal resolutions. However, by increasing the grid resolution, the approach seamlessly transitions ~~transforms seamless~~ ~~in~~to a traditional obstacle resolving Cartesian approach, as the interface eventually becomes sharply defined and imposes Neumann-boundary conditions on the pressure.

The paper is organized as follows: Section 2 provides a detailed ~~model~~ description of the model CAIRDIO, including the spatial discretization method. ~~Section 3 is dedicated to the evaluation of the model using idealized test cases and a more complex and realistic wind-tunnel dispersion experiment.~~ Section 3 contains numerical tests to demonstrate the diffuse obstacle discretization, the dynamic core and the parallel scaling capabilities. In Section 4, we present a model-evaluation study by simulating a realistic wind-tunnel dispersion experiment. Finally, in Section ~~4~~ 5, the benefits and limitations of the approach are summarized and concluded by an outlook for potential future applications.

2 Model description

2.1 Basic equations

The physical domain consists of an interspersed, stationary solid phase representing the buildings~~,~~ and a mobile fluid phase. The governing equations for the mobile phase are deduced from a simplified two-phase model by neglecting restoring forces. In a two-phase model, phase-fraction functions α_1, α_2 with $0 \leq \alpha_1 \leq 1$ and $\alpha_1 + \alpha_2 = 1$ are used to formulate the set of equations of both phases individually. The equation of motion of an incompressible phase is adopted from Drew (1983) (~~e~~Eq. 41, 45 therein). By setting the interfacial force density and surface tension to zero, the simplified momentum equation of the mobile phase (indicated with α_1) is written as:

$$\partial_t (\alpha_1 \rho \boldsymbol{u}) = -\nabla \cdot (\alpha_1 \rho \boldsymbol{u} \otimes \boldsymbol{u}) - \alpha_1 \nabla (\alpha_1 p) + p_I \nabla \alpha_1 + \nabla \cdot (\alpha_1 \mathbf{T}) + \alpha_1 \rho \boldsymbol{b}. \tag{1}$$

Here, the 3D velocity vector is denoted by $\boldsymbol{u}$, ρ is the density of air and p_I is the interface pressure, which reflect~~sing~~ Newton's third law of motion near a fixed wall. As in Kemm et al. (2020), p_I ~~it will be~~ is assumed ~~that it is~~ to be in equilibrium with the surrounding fluid pressure p. The stress tensor $\mathbf{T}$ ~~is the stress tensor, which in LES averaging~~ contains the contributions from subscale and surface fluxes in LES averaging. In this model, the implicit approach is used for spatial filtering (Schumann, 1975). Viscous stresses are neglected due to the high Reynolds numbers typically encountered in atmospheric flows. The sum of external body forces $\boldsymbol{b}$ ~~corresponds to the sum of external body forces, which also~~ contains the gravitational force and inertial forces resulting in a rotating frame of reference. The interface in our case is static, as buildings ~~are assumed~~ do not ~~to be affected by~~ respond to the flow. This makes it possible to multiply the equation of motion with $\alpha_1^{-1}\rho^{-1}$, to obtain the tendency equation in single-flow denotation. The reference density ρ_{ref} is ~~not allowed to change~~ kept constant in time ~~and is denoted with ρ_{ref} for the reference state, which makes sense~~ for an incompressible fluid. The full set of model equations reads:

$$\partial_t \boldsymbol{u} = -\alpha_1^{-1} \nabla (\alpha_1 \boldsymbol{u} \otimes \boldsymbol{u}) - \frac{1}{\rho_{ref}} \alpha_1^{-1} \alpha_1 \nabla p - \alpha_1^{-1} \nabla \cdot (\alpha_1 \mathbf{T}) - \boldsymbol{f} \times \boldsymbol{u} + \boldsymbol{g} \frac{\overline{\Theta}_v - \Theta_v}{\overline{\Theta}_v}, \tag{2}$$

$$\alpha_1^{-1}\nabla\cdot(\alpha_1\boldsymbol{u})=0, \tag{3}$$

$$\partial_t\Theta=-\alpha_1^{-1}\nabla\cdot(\alpha_1\boldsymbol{u}\Theta)+\alpha_1^{-1}\nabla\cdot(\alpha_1 k_h\nabla\Theta)+\alpha_1^{-1}S_\Theta, \tag{4}$$

$$\partial_t Q_v=-\alpha_1^{-1}\nabla\cdot(\alpha_1\boldsymbol{u}Q_v)+\alpha_1^{-1}\nabla\cdot(\alpha_1 k_h\nabla Q_v)+\alpha_1^{-1}S_{Q_v}, \tag{5}$$

$$\Theta_v=\Theta\left(1+0.61Q_v\right). \tag{6}$$

In the momentum equation (~~e~~Eq. 2), the body-force term ~~was~~ is replaced by the Coriolis term, ~~containing~~ with the Coriolis parameter $\boldsymbol{f}$ for a mean geographic latitude, and ~~with~~ the buoyancy term using the Boussinesq approximation. $\boldsymbol{g}$ is the gravity-acceleration vector in the local frame of reference~~,~~ and Θ_v the virtual potential temperature defined by Eq. 6.~~, and t~~The overbar denotes ~~for~~ the horizontal mean state. Eq. 3 is the continuity equation derived ~~by the same arguments~~ in an analogous way as the momentum equation from the original ~~equation~~ formulation in Drew (1983). The transport equation for scalars, like the potential temperature $\Theta_{\cancel{v}}$ and specific humidity Q_v, contains source terms from parameterized surfaces fluxes. These have to be multiplied with α_1^{-1}. The scalar field k_h is the eddy-diffusion coefficient for heat.~~, which arises from the spatial filtering.~~ Note that ~~in our case,~~ the combinations $\alpha_1^{-1}\nabla\cdot\alpha_1$ and $\alpha_1^{-1}\alpha_1\nabla$ can be identified as particular versions of the divergence and gradient operator, which incorporate diffusive boundaries. ~~It is also interesting to mention that~~ Using a staggered grid, the stencil of α_1 (face-centered) differs from α_1^{-1} (volume-centered)~~ on a staggered grid~~, so that the terms do not cancel each other out.

2.2 Computational grid~~ and diffuse boundaries~~

The computation uses a structured ~~hexaedral~~ Arakawa-C grid, with the ~~option for local grid stretching in all 3 dimensions. The~~ velocity components ~~are~~ being defined at the cell faces~~, whereas~~ and scalar fields ~~are~~ at the cell centers.~~ed, classifying the grid structure as Arakawa-C type.~~ Vertical coordinate transformation allows for a curve-linear grid in the physical space~~, which can be used to follow~~ to be adapted to a smoothly varying terrain function:

$$\tilde{x}=x,\quad \tilde{y}=y,\quad \tilde{z}=z-h(x,y).\cancel{,} \tag{7}$$

Here, z is the mean-sea level height and $h(x,y)$ the terrain-height function. ~~The first grid level matches the terrain function, and all e~~Elevated levels are simply given by adding a horizontally constant vertical increment to the first level.

The pressure gradient in terrain-following coordinates is ~~expands~~ modified to:

$$\nabla p = \tilde{\nabla} p - [\partial_x h(x,y) + \partial_y h(x,y)]\, \partial_z p. \tag{8}$$

~~The horizontal derivatives of $h(x,y)$ are discretized with second-order differences and linearly interpolated on the respective cell-faces, where needed.~~

~~For t~~ The divergence operator~~,~~ is applied on the contra~~-~~variant velocity components, which are ~~normal~~ parallel to the cell-face~~s~~ normal ~~are needed~~. ~~The horizontal components under the vertical coordinate transformation are indifferent, and the vertical contra-variant velocity~~ In our simple case, only the vertical contravariant velocity component ω differs from the co-variant non-transformed component. It is given by:

$$\omega = w - \partial_x h u - \partial_y h v. \tag{9}$$

Using Eq. 9, the advective tendency of a scalar q ~~can be~~ is written as:

$$\partial_t q = -u\partial_x q - v\partial_y q - [w - u\partial_x h - v\partial_y h]\, \partial_z q. \tag{10}$$

Similarly, the ~~divergence-free criterion~~ continuity equation ~~follows~~ in terrain-following coordinates follows from:

$$\partial_x u + \partial_y v + \partial_z (w - \partial_x h u - \partial_y h v) = 0. \tag{11}$$

Combining Eq. 11 and 8, the metric terms in the Laplace operator are obtained, which is later needed ~~in~~ for the pressure equation:

$$\begin{aligned} \triangle = & \tilde{\triangle} - \partial_x (\partial_x h \partial_z) - \partial_y (\partial_y h \partial_z) - \partial_z (\partial_x h \partial_x) \\ & - \partial_z (\partial_y h \partial_y) + \partial_z \left[(\partial_x h)^2 \partial_z \right] + \partial_z \left[(\partial_y h)^2 \partial_z \right]. \end{aligned} \tag{12}$$

As u, v, and w are maintained as the prognostic model variables and $\boldsymbol{g}$ is invariant under the given coordinate transformation, no metric terms arise in the buoyancy term. However, the horizontal averaging of Θ_v is carried out on z-isosurfaces. ~~requires a remapping of Θ_v from $\tilde{z} = const$ to $z = const$.~~ Therefore, Θ_v is remapped to an auxiliary vertical grid and the calculated tendency is remapped back to the computational grid.

2.3 Diffuse obstacle boundaries

The spatial discretization uses a finite volume method, which allows a consistent treatment of the diffusive obstacle ~~interface~~ boundaries. To consider t~~T~~he conservation of a scalar q ~~under phase partitioning~~ within two partitioned phases, the Gauss' theorem is formulated for a single grid-cell volume ΔV and its total surface area $\partial \Delta V$: ~~is formulated using the Gauss theorem:~~

$$\int\limits_{\Delta V} \partial_t \left[q_m \chi_m + q_s (1 - \chi_m) \right] \mathrm{d}V' = - \int\limits_{\partial(\Delta V)} \left[\boldsymbol{\eta_m} \cdot \boldsymbol{u_m} q_m + (1 - \boldsymbol{\eta_m}) \cdot \boldsymbol{u_s} q_s \right] \mathrm{d}\cancel{a}A'. \tag{13}$$

Here, subscript m refers to the mobile phase and subscript s to the solid phase for the building-interior. A' and V' are formal integration variables. χ_m is the volume-fraction function of the mobile phase and $\boldsymbol{\eta}_m$ the area-fraction function, over which the flux of the mobile phase is integrated. As already mentioned, the stationary solid phase is dropped, as it is $\partial_t \chi_m = 0$, $\partial_t q_s = 0$ and $\boldsymbol{u_s} = 0$. This simplifies the conservation form and finally leads to the particular differential form of the transport equation for the mobile phase:

$$\partial_t q_m = - \frac{1}{\chi_m \Delta V} \int\limits_{\partial(\Delta V)} \boldsymbol{\eta_m} \cdot \boldsymbol{u_m} q_m \, \mathrm{d}A = - \frac{1}{\chi_m} \nabla \cdot \boldsymbol{\eta}_m (\boldsymbol{u_m} q_m) =: -\nabla_m \cdot (\boldsymbol{u_m} q_m). \tag{14}$$

The subscript m was only briefly introduced here and will be dropped again, as only ~~one phase,~~ the mobile phase~~,~~ is of interest.

Using the Cartesian grid structure, the discrete flux-divergence ~~can be put in a discrete~~ results ~~form~~ from:

$$\begin{aligned} \nabla \cdot \boldsymbol{F} = \frac{1}{\chi \Delta V} [& (\eta_x \Delta A_x \cancel{f} F_x)^L - (\eta_x \Delta A_x \cancel{f} F_x)^R \\ & + (\eta_y \Delta A_y \cancel{f} F_y)^L - (\eta_y \Delta A_y \cancel{f} F_y)^R \\ & + (\eta_z \Delta A_z \cancel{f} F_z)^L - (\eta_z \Delta A_z \cancel{f} F_z)^R], \end{aligned} \tag{15}$$

where ΔV and $\Delta A_{x,y,z}$ are the cuboid volumes and face areas, respectively. The superscripts R and L refer to the left and right cell face for each dimension, respectively. F_x, F_y, and F_z are fluxes, whose concrete form is determined by the partial differential equation. Note that ~~for f_z,~~ the contra~~-~~variant flux has to be used for F_z.

The pressure gradient components on the cell faces are discretized with second-order accuracy. ~~For example, t~~The gradient components centred on the x-~~orientated~~ and z-orientated cell faces, ~~and z-orientated faces~~ respectively, are:

$$\partial_x p = \frac{2 \eta_x \Delta A_x}{(\chi \Delta V)^L + (\chi \Delta V)^R} \left(p^R - p^L \right) - \frac{1}{\Delta_x} \left(h^R - h^L \right) \mathbf{L}^{z \to x} \partial_z p, \tag{16}$$

$$\partial_z p = \frac{2\eta_z \Delta A_z}{(\chi\Delta V)^L + (\chi\Delta V)^R}\left(p^R - p^L\right), \tag{17}$$

where $\mathbf{L}^{z\to x}$ is the linear interpolation operator from a z-face to an x-face, and Δ_x is the cuboid size used for differencing the terrain function.

For a grid-conforming surface, the area fractions $\eta_{x,y,z} = 0$, ~~and it~~ from which ~~follows that~~ the required Neumann-boundary condition ~~is satisfied~~ follows. ~~Furthermore, if~~ In this case, a grid cell is completely surrounded by grid-conform~~ing~~ surfaces~~,~~ and the pressure value inside is decoupled from any ~~exterior~~ neighboring ~~grid cell~~ values, ~~which matches the~~ reflecting its physical meaninglessness~~ of such a value~~. For partially open semi-permeable cell-faces, the boundary condition is imposed ~~only~~ on a fraction of the cell face area only.

The scaling fields $\eta_{x,y,z}$ and χ ~~for the cell volumes and face areas intersected by buildings~~ are derived from geometric building data~~ sets~~. As an alternative to using terrain-following coordinates, it is possible to use diffuse boundaries for the terrain, in which case, the sub-surface is also represented by ~~an obstacle too~~ a geometric shape. Per definition, the volume-fraction field χ is expressed as the fraction of the building-free volume in each grid cell. For numerical reasons, however, χ is limited to a ~~value of about 0.01~~ small non-zero value. For well resolved buildings, the area-scaling fields $\eta_{x,y,z}$ ~~would be~~ are derived by calculating the intersections of the buildings with the grid-cell faces. For under-resolved buildings, however, this method ~~is very sensitive to the grid alignment,~~ fails to take the grid alignment into account. ~~and in certain cases, buildings are missed,~~ A resulting effect may be the entire missing of buildings if they do not intersect with ~~the~~ a particular cell face~~s~~, but nevertheless block the flow within a grid cell. Figure 1a) shows two possible scenarios, where grid cells are intersected by a building, which obviously blocks the flow in one dimension ~~entirely~~ completely but does not intersect with the cell faces oriented in the direction of the blocking~~ed flow direction~~. In order to ~~reliably capture such bottlenecks~~ capture such occurrences more reliably, a modified method to calculate the area fractions is used. In this method, t~~T~~he grid-cell volume is partitioned in slices, with the slicing planes being displaced along the dimension considered (e.g. the $x-$dimension for the $yz-$faces). The minimum value over ~~of~~ the free-volume fractions of ~~these~~ all slices is computed to define~~s~~ a ~~so-called~~ cell-area-scaling factor, which is then assigned to the cell face ~~being~~ in closer proximity to the obstacle. For a more robust capture of non-parallel building walls, the slicing can be repeated several times with a slight rotation of the plane normal. If, occasionally, ~~some~~ a cell face~~s~~ ~~are~~ is assigned to both values from the adjacent left and right grid cell, respectively, the minimum of both values is taken. For the resulting cell~~-~~face~~s~~ left without assignment, the geometric intersection with buildings is calculated as ~~suitable for~~ in the resolved case. Figure 1b) ~~shows~~ demonstrates ~~on a practical example~~ that ~~the~~ this method preserves the blocking effect of

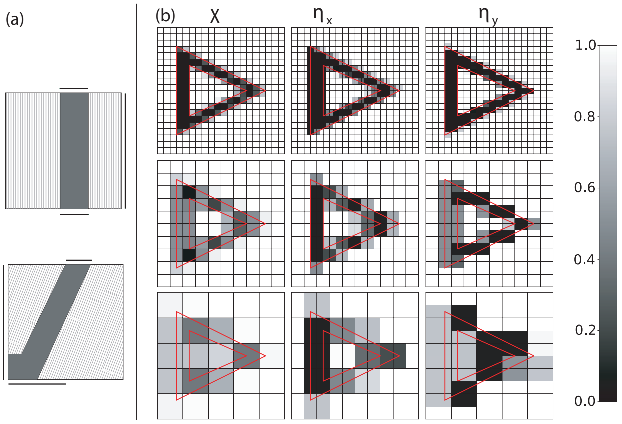

Figure 1. (a) Depiction of two different building sections (gray filled areas) inside a grid cell. The black lines mark the effectively blocked area of the respective side. The line pattern symboli~~s~~zes the slicing of the grid cell volume, which is ~~here~~ shown here only for the x-dimension. (b) Scaling factors for a complete building, now depicted as fields calculated for 3 different grid resolutions. χ is the volume-scaling field, and η_x, η_y are the horizontal components of the area-scaling field.

a triangular-shaped building~~, even at~~ for spatial resolutions, which ~~would be~~ are too coarse to resolve ~~the~~ individual building walls.

2.4 Numerics

2.4.1 Advection scheme

~~The main task in the discretization of the advection term in a finite-volume framework is the reconstruction of the cell-averaged fluxes on the faces to calculate the balance according to Eq. 15. It is noted, however, that even in the incompressible case, the flux-balance form differs from the required advective form, as there is a residual divergence originating from the approximate solution of the pressure equation.~~

$$\cancel{(\partial_t q)_{adv} = -\nabla\cdot(\boldsymbol{u}q) + q\nabla\cdot\boldsymbol{u}} \quad (18)$$

~~The reconstruction for a scalar reduces to several high-order 1-dimensional reconstructions of the cell-averaged value~~ ~~q~~ ~~on the cell faces. The fluxes are then obtained by multiplication with the exact momentum components, and are of the same spatial accuracy as the reconstructed scalars. For the reconstruction itself, upwind-biased stencils are used, requiring two reconstructions on each cell face for the two flow directions. Since the grid-spacing is not equidistant, the reconstruction coefficients have to be calculated in advance of the simulation as follows: Requiring the reconstruction to be~~ ~~n^{th}~~~~-order accurate,~~ ~~n~~ ~~cell averaged values are needed. Assuming the wind is blowing from the left (positive direction), the set of~~

~~values encompasses $q(j-r+s)$, $s\in[0,n-1]$, with $n \mod 2 = 1$, $r=(n-1)/2+1$ and j being the target cell-index for the flux-balance calculation. For the negative direction, it is $r=(n-1)/2$. In total, $n+1$ different values are needed.~~

~~The reconstruction itself is performed using the spatial derivative of the Lagrange polynomial, which fits the primitive function evaluated at the cell faces (see e.g. Shu, 1998):~~

$$P(x)=\sum_{s=0}^{n-1} q(j-r+s)\Delta_x(j-r+s)\sum_{m=s+1}^{n}\frac{\sum_{l=0,l\neq m}^{n}\prod_{p=0,p\neq m,l}^{n}(x-x_{j-r+p-1/2})}{\prod_{l=0,l\neq m}^{n}(x_{j-r+m-1/2}-x_{j-r+l-1/2})} \tag{19}$$

~~The coefficients have to be evaluated at the cell faces $j-1/2$ for the positive upwind direction, and $j+1/2$ for the negative one. The differences in parenthesis can be expressed in terms of the grid spacing. Instead of the geometric grid spacing, the effective grid spacing Δ_x^{eff}, which is derived from the scaling fields, is used as a pseudo grid. This ensures a decreased weighting of interpolation nodes within volume-compromised cells and prevents the scheme from interpolating the degenerated values inside closed cells.~~

$$\Delta_x^{eff}=\frac{2\chi}{\eta_x^L+\eta_x^R}\Delta_x \tag{20}$$

$$x_{j-1/2}-x_{j-r+p-1/2}=: \tag{21}$$

$$\begin{cases}\sum_{l=0}^{r-p-1}\Delta_x^{eff}(j-r+p+l) & r-q\geqslant 0\\ \sum_{l=0}^{p-r-1}-\Delta_x^{eff}(j+l) & p-r>0,\end{cases}$$

~~and~~

$$x_{j+1/2}-x_{j-r+p-1/2}=: \tag{22}$$

$$\begin{cases}\sum_{l=0}^{r-p}\Delta_x^{eff}(j-r+p+l) & r-p+1\geqslant 0\\ \sum_{l=1}^{p-r-1}-\Delta_x^{eff}(j+l) & p-r-1>0.\end{cases}$$

~~While the formulas permit reconstructions of arbitrary order, a 5^{th}-order reconstruction was found to give superior resolution to a 3^{rd}-order one, while still being computationally efficient. For any increase in the order, additional ghost layers need to be communicated. Additionally, limiting of the reconstructions is applied using a total-variation diminishing method of Sweby (1984).~~

~~This will ensure monotonicity for scalar advection. The two limited reconstructions q^+ and q^- are finally combined to give the numerical flux based on the propagation velocity u:~~

$$(uq)=0.5\left[u(q^+ + q^-)-||u||(q^+ - q^-)\right] \tag{23}$$

The advective tendency for a scalar q is obtained by adding the remnant velocity-divergence term from the approximate pressure solution to the flux-divergence term of the conservation law (Eq. 15):

$$(\partial_t q)_{adv}=-\nabla\cdot(\boldsymbol{u}q)+q\nabla\cdot\boldsymbol{u}. \tag{24}$$

The flux components are linear and given by the product of the reconstructed values $\tilde{q}$ at cell faces and the exactly given momentum components. We use an upwind-biased stencil of 5^{th} order, which results in two reconstructions $\tilde{q}^{+}$ and $\tilde{q}^{-}$ on each cell face. For an x-oriented face, the reconstructions are merged to the numerical flux by considering the wind direction:

$$(uq)_x = 0.5\left[u_x(\tilde{q}^{+}+\tilde{q}^{-}) - ||u_x||(\tilde{q}^{+}-\tilde{q}^{-})\right] \tag{25}$$

For non-uniform grid spacings, the coefficients of the reconstruction polynomials are pre-computed from the spatial derivative of the Lagrange polynomial which interpolates the primitive function at cell faces (see e.g. Shu, 1998). We use the pseudo-grid spacing calculated by $\Delta_x^{eff} = 2\Delta_x\chi/(\eta_x^L+\eta_x^R)$ instead of the computational grid spacing in order to automatically adjust the effective stencil width near obstacle boundaries. The behaviour of the pseudo-grid-based reconstruction of maximum 5^{th} order is demonstrated in Fig. 2 for a positive flow direction (left to right). Within shown the circular obstacle, the pseudo-grid spacing tends toward infinity, which effectively excludes such decoupled cells from interpolation. The resulting smaller stencils can be down-wind biased. An effective measure to prevent numerical instabilities is the application of a flux limiter (e.g. from Sweby 1984) near obstacle boundaries. To avoid non-physical results of positive scalars, a limiter has to be applied anyway. In the case of momentum advection, we use the absolute difference $|\eta_x(j-1)-\eta_x(j)|$ as a weighting function to merge the limited and unlimited reconstructions for obstacle-specific limiting. Note that this expression is upwind-biased (assuming a positive wind direction). In the free boundary layer, the difference is zero and no limiting is applied.

~~For momentum transport, t~~The routine for scalar cell-centered advection is ~~re-~~ repeatedly used to advect a left-faced u^l and right-faced value u^r for each momentum component (Hicken et al., 2005; Jähn et al., 2015), resulting in a total of 6 ~~routine calls~~ advection steps. ~~In contrast to scalar advection, monotonicity is generally not desired, as it has a detrimental impact on energy conservation and will interact with the subgrid model. To prevent wiggles near building walls and to increase numerical stability, only local limiting is applied at obstacle boundaries. For a reconstruction face at index position~~ $\cancel{j}$ ~~located near a diffusive boundary, a local weight can be taken as~~ $\cancel{\alpha_x^{+} = |(\eta_x(j-1)-\eta_x(j)|}$ ~~for the positive upwind direction, and~~ $\cancel{\alpha_x^{-} = |(\eta_x(j+1)-\eta_x(j)|}$ ~~for the negative direction. If~~ $\cancel{u_{Lim}^{+}}$ ~~is the limited reconstruction of~~ $\cancel{u^{+}}$~~, using the aforementioned weight~~ $\cancel{\alpha_x^{+}}$~~, the following merging results in a weighted limiting of the velocity component perpendicular to an adjacent building wall:~~

$$\cancel{u_{Limobs}^{+} = (1-\alpha_x^{+})u^{+} + \alpha_x^{+}u_{Lim}^{+}} \tag{26}$$

~~The scheme, if necessary, degrades only to first-order accuracy at obstacle boundaries, while in the free boundary layer, no additional numerical dissipation is introduced.~~

The final momentum tendencies are obtained by interpolation of two centered tendencies on the face:

$$\partial_t^{adv}u = \frac{\left(\chi\Delta V\partial_t^{adv}u^l\right)^R + \left(\chi\Delta V\partial_t^{adv}u^r\right)^L}{(\chi\Delta V)^R + (\chi\Delta V)^L} \tag{27}$$

~~Note that it is combined the right-faced advective tendency from the left grid cell and the left-faced tendency from the right grid cell (superscripts L and R, respectively).~~ Spatial accuracy of momentum advection is limited to the order of this interpolation procedure, which is of second order here.

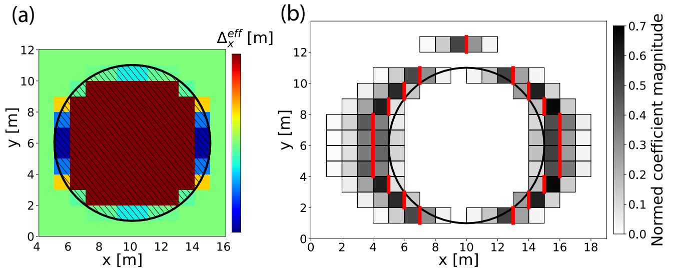

Figure 2. (a) Plot of the pseudo-grid spacing Δ_x^{eff} computed for a solid cylinder with diameter of $10\,\mathrm{m}$ using a uniformly constant grid spacing of $1\,\mathrm{m}$. Decoupled cells inside the cylinder are characterized by $\Delta_x^{eff} > 2$ in this plot. (b) Using same Δ_x^{eff} of (a), the reconstruction coefficients are computed for a 5-point upwind-biased stencil. The absolute values of the reconstruction coefficients are re-normed to one and depicted in shades of grey at individual reconstruction sites, which are marked by a vertical red bar. Stencil points are rendered invisible for values below 10^{-4}, as such have a negligible influence on the reconstructed value.

2.5 ~~Model integration, pressure correction method, and lateral boundary conditions~~

2.5.1 Model integration

In the incompressible-flow equations, the pressure gradient term is not directly coupled to a prognostic pressure equation. The projection method of Chorin (1968) is used to split the solution procedure in two steps. The first step integrates all the momentum tendencies, except the stated pressure gradient term, explicitly in time to obtain a predicted velocity $\tilde{\boldsymbol{u}}$:

$$\tilde{\boldsymbol{u}} = \boldsymbol{u}_{t_0} + (\partial_t \boldsymbol{u})_{ex}|_{t_0} \Delta t. \tag{28}$$

The final velocity estimate after one integration step $\boldsymbol{u}_{t_1}$ has to ful~~l~~fill the continuity equation:

$$\nabla \cdot \boldsymbol{u}_{t_1} = 0. \tag{29}$$

The ~~not yet known~~ required corrective tendency ~~is~~ has to be associated with the neglected pressure gradient ~~$\partial_t \tilde{\boldsymbol{u}} = -\frac{1}{\rho_{ref}} \nabla p|_{t_1}$~~, which is formally integrated with an Euler-backward step to obtain the final velocity at $t_1 = t_0 + \Delta t$ ~~: Applying the divergence operator on both sides gives:~~

$$\cancel{\nabla \cdot \boldsymbol{u}_{t_1} = \nabla \cdot \tilde{\boldsymbol{u}} - \frac{\Delta t}{\rho_{ref}} \triangle p|_{t_1}.} \tag{30}$$

~~Since, as mentioned, the left side has to be zero, one obtains the well-known Poisson equation for pressure, which is to be solved algebraically:~~

$$\boldsymbol{u}_{t_1} = \tilde{\boldsymbol{u}} - \frac{\Delta t}{\rho_{ref}} \nabla |p_{t_1}. \tag{31}$$

By applying the divergence operator on both sides and requiring that $\nabla \cdot \boldsymbol{u}_{t_1} = 0$, the well-known Poisson equation for pressure is obtained:

$$\frac{\rho_{ref}}{\Delta t} \nabla \cdot \tilde{\boldsymbol{u}} = \triangle p|_{t_1}. \tag{32}$$

After algebraic solution of this equation, t~~T~~he final state ~~is~~ can now be composed of the fractional tendencies:

$$\boldsymbol{u}_{t_1} = \boldsymbol{u}_{t_0} + \Delta t \left[(\partial_t \boldsymbol{u})_{ex}|_{t_0} - \frac{1}{\rho_{ref}} \nabla p|_{t_1} \right]. \tag{33}$$

Equation 33 is ~~also an example of a~~ only first-order accurate in time ~~Euler method~~. ~~Higher-order multistage Runge-Kutta (RK) methods have the advantages of increased temporal accuracy and larger time stepping. The numerical stability of the integration in most practical examples is constrained by the advective and pressure-gradient tendency. Therefore, all the remaining terms are considered as the minor tendencies, and are evaluated only at every first stage. Different RK methods were tried in our model framework. It was found that the 2^{nd}-order midpoint rule (MP-RK2) and the strong-stability preserving 3^{rd}-order scheme (SSP-RK3) performed reasonably well. Using Taylor expansion, Karam et al. (2019) showed that RK2 and RK3 schemes can preserve their order of accuracy in spite of using just one pressure solve at the final stage. For all the intermediate projection steps, 1^{st}- and 2^{nd}-order accurate pressure estimates are interpolated from values at previous time steps. In practical examples, the computational savings were partially sacrificed by a decreased stability of the schemes, requiring smaller time steps. We found that MP-RK2 maintains stability up to a Courant number of $C = 0.3$, and the SSP-RK3 scheme up to $C = 0.7$ with one final pressure solve. Based on this, SSP-RK3 will be used for all of the applications in this paper and in future.~~ For higher accuracy, it is instead used a 3^{rd}-order strong-stability preserving Runge-Kutta scheme (SSP-RK3) for the advective and pressure-gradient tendencies, which also allows to use larger time steps. The pressure to correct the first two intermediate states is extrapolated from values given at previous time steps, and only for the final stage, the pressure solver is applied (Karam et al., 2019). We found that this combination supports stable integration up to a Courant number of $C = 0.7$.

2.5.2 Pressure solution

The discretization of the Laplace operator **P** in the Poisson equation (Eq. 32) is obtained by the product of the discrete divergence ~~matrix~~ **D** and gradient ~~matrix **G** defined by the discrete forms~~ in sparse matrix form. **D** is defined by the flux-balance in Eq. 15. Combining the operators to the pressure equation, the following sparse linear system is obtained:

$$\mathbf{P}p = \frac{1}{\Delta t}\mathbf{D}\tilde{u} =: b, \tag{34}$$

where $\tilde{u}$, p and b are the one-dimensional expanded arrays of the corresponding structured fields. Eq. 34 is solved with a geometric multigrid method in parallel using domain-decomposition in two dimensions. The multigrid algorithm consists of applying a smoothing method of choice which is accelerated by coarse-grid corrections. Therefore, a hierarchy of coarse grids is employed (Brandt and Livne, 2011). 3~~-d~~D coarsening of the grid is carried out by agglomeration of 8 grid cells to form a coarse grid cell of the next-level grid. For ~~odd~~ uneven grid sizes, a plane of grid-cells with respective orientation is left uncoarsened. This particular multigrid used in combination with finite volume discretizations is often referred to as cell-centered multigrid in literature (Mohr and Wienands, 2004).

Particular challenges to the multigrid algorithm include grid stretching and, in our case, non-smoothly varying coefficients associated with the diffus~~iv~~e boundaries, both resulting in coefficient anisotropy. An odd grid size results in coefficient anisotropy of the coarse grid operators. ~~Furthermore, Neumann boundary conditions result in a reduced smoothing efficiency near boundaries.~~ In such cases, plane smoothers are ~~much more adequate~~ often much more robust than their point-wise pendants (Llorente and Melson, 2000). Nevertheless, most of the difficulties ~~were~~ could be overcome by applying less elaborated methods in the current model.

Based on smoothing analysis, Larsson et al. (2005) give a condition for the optimal location of an uncoarsened plane in the case of odd grid sizes. ~~For an odd grid size in any direction, the~~ Galerkin coarse-grid approximation ~~(GCA)~~ can result in a better approximation of the coarse-grid operator in this case, while discretization coarse-grid approximation can be more efficient for even-sized grid dimensions. Our algorithm employs a combination of both methods on different grid levels. ~~is much more robust than re-discretization of the Poisson equation. In GCA, the coarse-grid operator is formed algebraically by applying interpolation operators from the left (restriction) and right (prolongation) on the original matrix. The original stencil size of 7 points (without using terrain-following coordinates) is only preserved for piece-wise constant interpolation for both restriction and prolongation. In this case, it is necessary to multiply with a factor of 1/2 to compensate for the poor approximation quality (Braess, 1995). Trilinear prolongation would give an adequate approximation quality for constant-coefficient operators, but it failed in our case of highly discontinuous media. As a compromise, the trilinear interpolation operator can be modified to approximate piece-wise constant interpolation near diffusive boundaries. As a drawback of trilinear interpolation, the coarse-grid stencil encompasses 27 points which increases numerical costs of coarse-grid corrections.~~

~~The smoothing method employed on each grid has to be efficient for moderate coefficient anisotropies.~~ Yavneh (1996) found that for smoothing, successive over-relaxation (SOR) is generally superior to Gauss Seidel smoothing (even for isotropic coefficients), and he also derived approximately optimal over-relaxation factors for SOR with red-black ordering applied in multigrid for the solution of anisotropic elliptic equations. ~~An advantage of the red-black ordering is the complete vectorization and parallelization of the algorithm, while a disadvantage is the not optimal cache efficiency, as the computation grid is accessed twice in each iteration (Di et al., 2009). A more cache efficient SOR method provides the standard lexicographic ordering, which however suffers from a degradation toward the less efficient Jacobi relaxation at subdomain boundaries in the parallel implementation.~~

In our implementation, also sparse-approximate inverse (SPAI) matrices (Tang and Wan, 2000; Bröker and Grote, 2001; Sedlacek, 2012) are available as ~~S~~suitable alternatives ~~for anisotropic problems~~ to SOR ~~are sparse-approximate inverse (SPAI) matrices as smoothers (Tang and Wan, 2000; Tang and Wan, 2001; Tang and Wan, 2012)~~. ~~Depending on the approximation quality of SPAI, which can be controlled by the sparsity pattern and consequently the number of allowed non-zeros, the efficacy of the smoother can be flexibly enhanced in order to tackle the difficult Poisson problem with varying coefficients. Since the Poisson matrix is not time dependent, it pays off to invest computational resources in a good approximation, as it is only necessary once at the beginning of the simulation.~~ These smoothers can inherently consider coefficient anisotropy through the algebraic method by which they are derived. Moreover, a variable number of non-zeros in the matrix allows a flexible control of the approximation quality and smoothing efficacy.

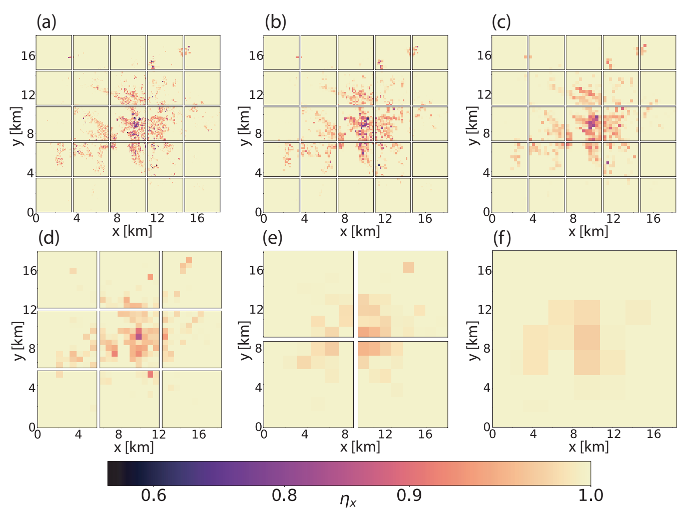

Figure 3. Example of a horizontal multigrid domain decomposition, involving 6 grid levels. Depicted are the area-scaling factors of yz-faces for the city of Leipzig at different resolutions of (a) 80 m, (b) 160 m, (c) 320 m, (d) 640 m, (e) 1280 m, and (f) 2560 m. The scaling factors are needed in the discretization of the Poisson equation. On the coarsest grid, a single processor is left for the computation.

2.5.3 Lateral boundary conditions

Before each pressure correction step, ~~global~~ lateral boundary conditions ~~for the next time step are already updated for~~ of the intermediate velocity field $\tilde{\boldsymbol{u}}$ are updated. ~~This approach naturally leads to a homogeneous-zero Neumann boundary condition for the pressure, which is shown in the following. We require that the updated velocity field satisfies~~ The update has to ensure global mass conservation:

$$\oint\limits_{\partial V} \frac{\rho_{ref}}{\Delta t} \tilde{\boldsymbol{u}} \cdot \boldsymbol{n} \, \mathrm{d}\cancel{a}A' = 0. \tag{35}$$

This expression implies a homogeneous-zero Neumann boundary condition for pressure at all lateral boundaries, as the already updated boundary values should not be changed by the projection:

~~Using Eq. 35 as the source term of the pressure equation (Eq. 32) and applying Stokes theorem, one arrives at a Neumann condition for the pressure:~~

$$\cancel{\oint_{\partial V} \frac{\rho_{ref}}{\Delta t} \tilde{\boldsymbol{u}} \cdot \boldsymbol{n} \, \mathrm{d}a = \int_V \frac{\rho_{ref}}{\Delta t} \nabla \cdot \tilde{\boldsymbol{u}} \, \mathrm{d}V = \int_V \nabla \cdot \nabla p \, \mathrm{d}V = \oint_{\partial V} \nabla p \cdot \boldsymbol{n} \, \mathrm{d}a = 0} \tag{36}$$

~~Here $\boldsymbol{n}$ is the unit normal vector on the boundary surface. Since the tendencies of the already updated boundary values are zero, no projection is applied, which corresponds to the homogeneous-zero condition:~~

$$0 = \rho_{ref} \frac{\partial \tilde{\boldsymbol{u}}}{\partial t} \cdot \boldsymbol{n} = \nabla p \cdot \boldsymbol{n}. \tag{37}$$

~~Note that by already updating the boundary condition for $\tilde{\boldsymbol{u}}$, the pressure boundary condition was homogenized by attributing the in-homogeneity to the source term $\nabla \cdot \tilde{\boldsymbol{u}}$. An important remark to Eq. 37 is concerning the special case, when terrain-following coordinates are used. By requiring $\partial_t \omega = 0$ for the contra-variant vertical velocity, the pressure boundary condition for the top- and bottom-domain boundaries is given by:~~

$$\cancel{0 = \partial_z p - \partial_x h \partial_x p - \partial_y h \partial_y p} \tag{38}$$

~~In this most general case, the projection still allows variations in the velocity, and it requires the solution of an additional linear equation (or an additional grid plane in the pressure equation). In order to keep the boundary velocity vector fixed and to prevent numerical expenses, it is used the trivial condition at the top and bottom boundaries:~~Here, $\boldsymbol{n}$ is the unit normal vector on the boundary surface. A more general case arises with the use of terrain-following coordinates. By requiring not only $\partial_t \omega = 0$, but additionally $\partial_t w = 0$ at the bottom and top of the computation domain, the following boundary condition follows at these boundaries:

$$\partial_z p = 0 \tag{39}$$

$$\partial_x p = \begin{cases} 0 & \partial_x h \neq 0 \\ \text{not specified} & \text{else} \end{cases}$$

$$\partial_y p = \begin{cases} 0 & \partial_y h \neq 0 \\ \text{not specified} & \text{else} \end{cases} \tag{40}$$

In the discrete gradient operator, homogeneous Neumann boundary conditions are implemented by setting all coefficients associated with the node to zero where the condition applies.

The ~~not yet specified~~ boundary condition for the velocity field has to be compatible with a dynamic mesoscale forcing and also ~~with the integrability condition of~~satisfy Eq. 35. ~~The workflow is therefore to first dynamically~~Firstly, inflow and outflow regions~~,~~ are dynamically determined in order to impose separate appropriate boundary conditions.~~, and then add a correction flux to the outflow regions to balance the total inflow-region flux. The o~~Outflow regions are ~~determined~~characterized by convective transport out of the domain. Therefore, a simple normalized convective transport speed $C_\perp = \frac{\Delta t}{\Delta x} \boldsymbol{u} \cdot \boldsymbol{n}$ is computed. ~~$C_\perp > 0$, where $C_\perp$ is a normalized convective transport speed out of the domain. $C_\perp$ is evaluated at interior grid points and time step t. For simplicity, it is taken $C_\perp = \frac{\Delta t}{\Delta x} \boldsymbol{u} \cdot \boldsymbol{n}$, however~~Note that more elaborate formulations for $C_\perp$ exist. ~~The transport velocity~~$C_\perp$ is further bounded to ~~$0 \leq C_\perp \leq 1$~~$[0,1]$ for numerical reasons. It is then $C_\perp > 0$ for outflow regions. ~~This ensures numerical stability of the prognostic radiation equation applied to outflow ghost cells. As proposed by Miller and Thorpe (1981), first order upwinding is used:~~For such regions, the radiation boundary condition by Miller and Thorpe (1981) is imposed:

$$\boldsymbol{u}_{l+1}^{t+1} = \boldsymbol{u}_{l+1}^{t} - C_\perp \left(\boldsymbol{u}_{l+1}^{t} - \boldsymbol{u}_{l}^{t} \right). \tag{41}$$

The order of the spatial indexing l is in normal direction to the boundary and not to confuse with the standard interior indexing. The index $l+1$ corresponds to the first ghost cell. At the remaining inflow boundaries, Dirichlet conditions are specified. ~~Figure 4 shows that the outflow boundary condition with the proposed convective transport speed is well suited to our incompressible model even for highly unsteady flows, like the depicted vortex street in the wake of a cylinder. Individual vortices are not visibly reflected at the boundary, and also in the temporal mean, based on Fig. 4b, the influence of the boundary is not discernible.~~

Instead of the flexible inflow-outflow condition, a Rayleigh damping layer can be used as another prognostic tendency near the domain top:

$$\partial_t^{dmp} q = -\frac{R(z)}{\tau}(q - q_0). \tag{42}$$

Eq. 42 can be applied to gradually relax any prognostic variable toward a prescribed horizontal mean state at the top boundary. R is a ramp function with values between $[0, 1]$, τ the damping time scale and q_0 the prescribed boundary value.

~~The final step is to impose global mass conservation, for which a correction flux $\dot{m}^d$ is integrated for each dimension d separately:~~

$$\cancel{\int_{A^d_{DIR}} \rho_{ref} \boldsymbol{u}_{l+1} \cdot \boldsymbol{n} \, \mathrm{d}a + \int_{A^d_{RAD}} \rho_{ref} \boldsymbol{u}_{l+1} \cdot \boldsymbol{n} \, \mathrm{d}a = -\dot{m}^d, \; d \in \{x, y, z\},} \tag{43}$$

~~where A_{DIR} is the surface area on which a Dirichlet condition is imposed, and A_{RAD} the remaining surface area with the radiation condition imposed. It is further $\sum_d A^d_{DIR} + A^d_{RAD} = \partial V$ the total domain-bounding area. The correction fluxes are converted to a corresponding correction speed $u^d_{\dot{m}}$, which is added to the boundary-perpendicular velocity component on A_{RAD}. The mass flux is distributed over the radiation-condition area by using for example $C_\perp$ in a weighting function:~~

$$\cancel{u^d_{\dot{m}} = \frac{\dot{m}^d \, \mathrm{sign}\,(a)}{\rho_{ref}} \frac{C_\perp}{\int_{A^d_{RAD}} C_\perp \, \mathrm{d}a}} \tag{44}$$

~~Attention must be paid to the sign of the correction velocity, as Eq. 44 is multiplied by a negative sign for right-hand sided boundaries. When using terrain-following coordinates, it is the contra-variant vertical flux perpendicular to the bounding surface and used in Eq. 43. The correction speed is simply added to the covariant component w~~.

Final mass conservation is enforced by making sure that the total inflow-mass flow is exactly balanced by the total outflow-mass flow. This is accomplished by computing an averaged correction velocity from the mass-flow difference. In the case, each spatial dimension is considered independently from each other, this results in 3 different correction velocities. The correction velocities are finally added to the boundary-perpendicular velocity component at the outflow regions.

Figure 4 shows that the outflow boundary condition with the proposed convective transport speed is well suited to our incompressible model even for highly unsteady flows, like the depicted vortex street in the wake of a cylinder. Individual vortices are not visibly reflected at the boundary, and also in the temporal mean, based on Fig. 4b), the influence of the boundary is not noticeable.The flexible boundary condition can principally be applied to any other scalar quantity, although, specifying Dirichlet conditions for advected scalars was found to be well suited.

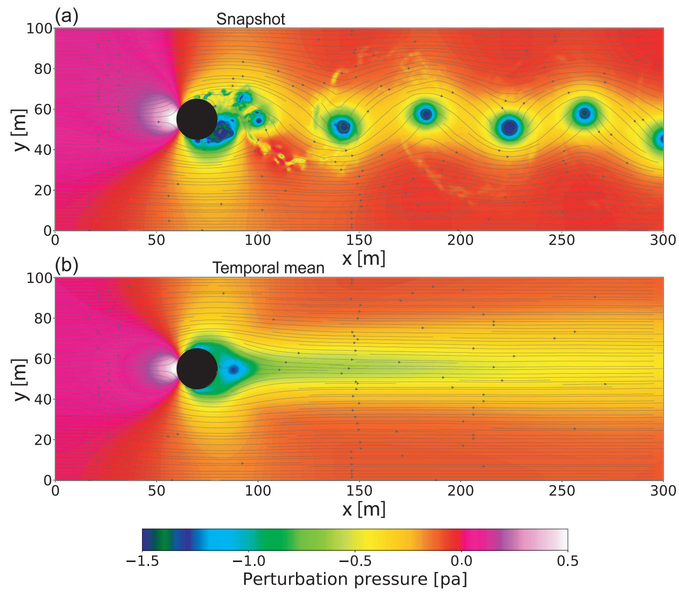

Figure 4. LES of 3D flow past a cylinder. The horizontal grid spacing is uniformly $0.5\,\mathrm{m}$. The cylinder has a diameter of $40\,\mathrm{m}$. The approaching flow is laminar with $u = 1\,\mathrm{m\,s^{-1}}$. Flexible Dirichlet-radiation conditions are imposed on all horizontal domain-boundaries, while periodic boundary conditions are used in z-direction. The contour plot depicts the pressure and the streamlines the horizontal velocity field. (a) shows a frame at the instance during a sharply defined vortex is about to cross the right boundary, (b) shows the temporal mean over a representative simulation period.

2.6 Physical processes

2.6.1 Subgrid model

For numerical simplicity and efficiency, a static Smagorinsky subgrid model is used (Deardorff, 1970). Since the atmospheric model is operated in the limit of infinite Reynolds numbers, the principal purpose of the subgrid model is to ~~stabilize the numerical simulation through an additional amount of energy dissipation at the shortest wavelengths~~dissipate enough energy at the shortest wavelengths to obtain a physically realistic energy cascade. In our case, the subgrid model also has to compensate for the under-resolved vertical mixing of tracers within the urban boundary layer. ~~Generally speaking, the magnitude of the subgrid fluxes shall be only a small fraction of those of the resolved fluxes, so that any potential non-physical assumptions in the subgrid model have little influence on the resolved fields. This is a prerequisite for large eddy simulations, and is one of the main reasons, why the static Smagorinsky model, despite its obvious short comings, is still a popular choice.~~

~~The Smagorinsky model relates the subgrid turbulent fluxes to the resolved rates of strain $s_{x,y}$:~~ In the Smagorinsky model, the rates of strain $s_{x,y}$ are approximated by the velocity gradients:

$$s_{x,y} = \frac{1}{2}\left(\partial_y u + \partial_x v\right). \tag{45}$$

The subscripts x, y refer to the spatial components. The turbulent fluxes are derived in analogy to the viscous fluxes by assuming an eddy viscosity ϵ_k:

$$u'_x u'_y = 2\epsilon_{x,y} s_{x,y} \tag{46}$$

~~The terms in Eq. 45 and Eq. 46 are cell averaged values, and overbars are neglected for convenience.~~ The often additionally mentioned anisotropic residual-stress tensor is ignored in the given incompressible case. In the most simple case, $\epsilon_{x,y}$ ~~is the eddy viscosity, which for numerical efficiency,~~ is also diagnosed from the rates of strain ~~instead of solving an additional prognostic equation for the turbulent kinetic energy~~. $\epsilon_{x,y}$ is denoted in tensor form, as an anisotropic mixing length $l_{x,y}$ is used to reflect grid anisotropy:

$$\epsilon_{x,y} = l_{x,y}^2 |\mathbf{S}| f = \left(c_s \Delta_{x,y}\right)^2 |\mathbf{S}| f_s \tag{47}$$

$|\mathbf{S}|$ is the Frobenius norm of the ~~stress~~strain-rate tensor. c_s is the Smagorinsky constant, which is fixed in a static model. Tests with a boundary layer simulation revealed that the range $0.1 < c_s < 0.15$ gives good results in combination with the 5^{th}-order upwind scheme.~~discretization values of $0.1 < c_s < 0.15$ give good results. Finally, the~~Grid anisotropy enters via $\Delta_{x,y}$ which is ~~related to the grid spacing and~~ further modified by half the mean distances to walls h_x and h_y, respectively:

$$\Delta_{x,y} = \min\left(\sqrt{\Delta_x \Delta_y}, 1.8h_x, 1.8h_y\right). \tag{48}$$

~~h_x is half of the mean distance between walls orientated in the x-direction.~~

The function f_s introduces the influence of the stratification on the eddy viscosity. It is assumed:

$$f_s = \begin{cases} 0 & Ri \geq 0.25 \\ \sqrt{1 - 16Ri} & Ri < 0 \\ (1 - 4Ri)^4 & else, \end{cases} \tag{49}$$

with the Richardson number Ri:

$$Ri = \frac{g\partial_z \Theta_v}{\Theta_v |S|^2}. \tag{50}$$

For scalar diffusion, the eddy viscosity is divided by the turbulent Prandtl number, which is assumed to be $Pr = 2/3$ here.

If not mentioned otherwise, the appearing spatial derivatives are discretized with second-order differences. To obtain the strain rate components and the eddy viscosity on different stencil points (cell faces areas and cell centers), linear interpolation is used. The sub~~scale~~grid tendency is ~~approximated~~formed by the divergence of the diffusive fluxes. Shifted grids are introduced t~~T~~o account for the definition of the velocity components on the cell faces~~, shifted grids are introduced~~. For example, diffusion of the u-component requires a grid shifted by $\Delta_x/2$, for which the scaling fields are also obtained by linear interpolation. The diffusive fluxes are given by:

$$\cancel{f}F_{x,y} = 2\epsilon_{x,y}s_{x,y}. \tag{51}$$

For diffusion of the u-component, the fluxes in the 3 spatial directions are $\cancel{f}F_{x,x}$, $\cancel{f}F_{x,y}$ and $\cancel{f}F_{x,z}$. Those of the other components are obtained by permuting the subscripts. For a scalar quantity q, the required fluxes are $\cancel{f}F_{x,x}$, $\cancel{f}F_{y,y}$ and $\cancel{f}F_{z,z}$, ~~wherein~~ with the rates of strain ~~are~~ being replaced by the gradient components.

2.6.2 Surface fluxes

Surface fluxes for momentum, heat and moisture are parameterized, using Monin-Obhukov similariry theory (Louis, 1979). An expression for t~~T~~he vertical transfer coefficient C_z ~~is given~~can be obtained by transforming the logarithmic~~-~~wind law:

$$C_z = \frac{k^2}{\log^2(z/z_0)} \tag{52}$$

$k = 0.4$ is the Von Kármán constant, z_0 the surface roughness length, and z the height difference from the modeled surface to the grid level where the parameterization is evaluated. ~~In order to alleviate the often encountered problem with the log-layer mismatch (Yang et al., 2017), it is advantageous to take the second or third grid level above respective surface, since close to the surface turbulence is not adequately resolved.~~

The momentum sinks from horizontal surfaces are:

$$\frac{\partial u'w'}{\partial z} = -\frac{A_z}{\Delta V} f_m C_z u \sqrt{u^2 + v^2} \tag{53}$$

and

$$\frac{\partial v'w'}{\partial z} = -\frac{A_z}{\Delta V} f_m C_z v \sqrt{u^2 + v^2}. \tag{54}$$

Analogously, the source terms for heat and moisture from horizontal surfaces are:

$$\frac{\partial \Theta' w'}{\partial z} = -\frac{A_z}{\Delta V} f_h C_z \left(\Theta - \Theta^s\right) \sqrt{u^2 + v^2} \tag{55}$$

and

$$\frac{\partial Q_v' w'}{\partial z} = -\frac{A_z}{\Delta V} f_h C_z \left(Q_v - Q_v^s\right) \sqrt{u^2 + v^2}. \tag{56}$$

Θ^s is the surface potential temperature, and Q_v^s the surface specific humidity. A_z is the total exposed horizontal surface within the grid cell, and ΔV the effective cell volume. f_m and f_h are stability functions, and z_0 the surface roughness length. ~~f_m is based on the Bulk Richardson number, which is the fraction of buoyant to shear energy production and calculated as:~~We adopt the expressions given in Doms et al. (2013) to calculate f_m and f_h for land surfaces.

$$\cancel{RiB = \frac{g(\Theta - \Theta^s)z}{\Theta^s(u^2+v^2)}} \tag{57}$$

~~In stable conditions, $RiB > 0$, and the stability functions are empirically determined by Doms (2011) for land surfaces:~~

$$\cancel{f_m = \frac{1}{1+10RiB(1+5RiB)^{-0.5}}} \tag{58}$$

$$\cancel{f_h = \frac{1}{1+15RiB(1+5RiB)^{0.5}}} \tag{59}$$

~~Conversely, in unstable conditions $RiB < 0$, and~~

$$\cancel{f_m = 1 + \frac{10|RiB|}{1+75C_z\left[\left(\frac{z}{z_0}\right)^{0.33} - 1\right]^{1.5}} \sqrt{|RiB|}} \tag{60}$$

$$\cancel{f_h = 1 + \frac{15|RiB|}{1+75C_z\left[\left(\frac{z}{z_0}\right)^{0.33} - 1\right]^{1.5}} \sqrt{|RiB|}} \tag{61}$$

Sources and sinks from vertical building walls are treated similarly, ~~with the exception that~~but the stability function is set to unity in this case. For x-orientated surfaces, z is replaced by half of the average distance between surfaces in the equation for the transfer coefficient. Analogously, A_z is replaced by A_x for the total projected surface area with x-orientation. The surface fields Θ^s and Q_v^s ~~can be considered as~~ are part of the external forcing and have to be provided either by the hosting mesoscale model or field-interpolated measurements.

2.6.3 Turbulence recycling scheme

Wu (2017) gives an overview of various turbulence generation methods to provide turbulent inflow conditions. Among the different methods, a turbulence recycling ~~scheme was implemented~~is used in ~~the~~our model, as it is computationally efficient and can be applied to a wide range of different domains and flow types. ~~One peculiarity of the used scheme is that the recycling plane can be placed at an arbitrary distance to the inflow boundary within the computation domain, and all 4 horizontal boundaries are considered as potential inflow boundaries, unless periodic boundary conditions are specified. The only requirement is that the plane distance is at least several integral length scales to prevent a spurious periodicity of the recycled turbulent features. In some cases, it may even practical to place the recycling planes near the respective opposite boundaries, if the inflow conditions shall be those from an urban boundary layer. In this case, no extra development fetch is needed.~~In our implementation, turbulence can be extracted within a maximum of 4 vertical planes, each one properly displaced parallel to a particular inflow boundary. The resulting domain fetch for turbulence recycling has to extend several integral length scales in order to prevent a spurious periodic pattern of the recycled turbulent features.

At each model time step, a horizontal filter is applied on the velocity components within the recycling plane. In the case of coupling with a mesoscale model, ~~By setting~~ the ~~characteristic~~ filter width w_r is set to just below the spatial resolution of the host model in order to spare ~~to the integral length scale, the~~ mesoscale variations ~~are spared, which is important in case of spatially and temporally varying boundary conditions~~. Vertical filtering is not feasible due to the strong vertical wind shear within the boundary layer. The filtered velocity component is subtracted to obtain the small-scale fluctuation component:

$$u(z,y)' = u(z,y) - < u(z,y) >_{w_r} . \tag{62}$$

Equation 62 assumes a boundary perpendicular to the flow in x-direction. ~~Next, t~~The turbulent intensity is re-scaled to the target value, after which the fluctuation field can be added to the inflow boundary field u_{in} of the large scale flow u_{ls}.

$$u_{in}(z,y) = u_{ls}(z,y) + min\left[a_{max}, \frac{||u'_{tar}||_2(z)}{||u'||_2(z)}\right] u'(z,y) \tag{63}$$

a_{max} is used to limit the artificial amplification of turbulence shortly after model initialization.

The filtering operation, as well as the calculation of the turbulent intensities require communications in the parallel implementation. ~~In order to keep a maximum degree of parallelism in the model, decentralized filtering is used, instead of the much simpler method of transferring all the data to a root node.~~ For optimal parallel scaling, filtering is performed on each subdomain containing a part of the recycling plane instead of the much simpler method of filtering all the data with a single processor. A box-shaped filter is used to minimize the amount of communication in the parallel filtering. ~~Before filtering, additional ghost cells are exchanged, whose communication effort can be substantial for large filter widths. In this regard it is advantageous and adequate to use an efficient box filter.~~ A final communication ~~is potentially~~ may be necessary to transfer the ~~data~~ recycled turbulence to the inflow boundary~~, if the recycling plane is located on another subdomain~~. ~~Overall, d~~Despite the communication-intense filtering ~~overload~~, the computational costs of the recycling scheme were found to be ~~only~~ 1% to 2% of total costs on average.

2.7 Programming language

The presented model CAIRDIO v1.0 is written in Python, a programming language which facilitates a straightforward implementation of numerical methods, code compactness, and code readability. Python packages like NumPy, SciPy, and mpi4py make the programming language also suitable for high-performance computing. Our model implementation can particularly benefit from NumPy, as all time critical numerical routines (e.g. all the routines for the computation of explicit tendencies) support vectorized computations. This is an inherent property of the diffuse interface approach, as all grid cells, except for the ghost cells at sub-domain boundaries, are computation cells and treated in the same manner. All tendencies are formulated in flux-divergence form, and as a result, obstacle boundaries have not to be specified particularly. For the multigrid pressure solver, SciPy provides efficient data structures, methods, and functions for sparse-matrix algebra. Parallel computation is realized through a 2D-domain decomposition, with each processing node running its own full-fledged simulation. Message passing interface (MPI) is used to successively exchange data between subdomains.

3 Numerical tests

~~A series of simulations of different complexity is carried out in order to assess the model accuracy and demonstrate the capabilities of the numerical core. The first model experiment is an advection test taken from Calhoun and LeVeque (2000). A tracer is advected within a rotating annulus. Due to to the large number of intersected grid cells in manyfold ways, this test can be considered as challenging for the empirically determined order of convergence. In the second test, which is also reported in Calhoun and LeVeque (2000), a wave of a test tracer is advected through an irregular obstacle field. The stationary wind field is a numerically-approximated potential-flow solution obtained with a single projection step. A sensitivity study is performed to determine the grid-spacing sensitivity of the advection routine in combination with the projection method. The third basic example to evaluate the dynamic core is the rising bubble simulation of Wicker and Skamarock (1998). While the benchmark simulation is compressible, it will be determined how well the anelastic approximation in this model compares to it. The actual evaluation part is completed with the simulation of the wind-tunnel experiment "Michelstadt" (Berbekar et al., 2013). It provides a high-quality standard dataset for LES-type dispersion model evaluation. As a last example, which is orientated towards a more practical application, the models capability is demonstrated to simulate meteorology and air-pollution dispersion under non-neutral stratification over non-uniform terrain.~~

Some numerical tests are conducted in order to examine grid-sensitivity of the diffuse obstacle interface, the dynamic core and parallel efficiency of the model. To test the diffusive obstacle interface, a similar advection test as reported in Calhoun and LeVeque (2000) is performed. In order to show that the dynamic core can reproduce the expected evolution of an idealized setup, the rising-bubble experiment of Wicker and Skamarock (1998) is conducted once again. It also provides a benchmark to compare the anelastic approximation with a fully compressible model used in the original study. Finally, a third test is conducted to demonstrate the strong scalability on a high-performance computing platform.

3.1 ~~Annulus advection test~~

~~In the advection test described in Calhoun and LeVeque (2000), a circumferential flow field inside an annulus with the inner radius $R_1 = 0.75$ and outer radius $R_2 = 1.25$ is defined by the following potential-flow function:~~

$$\Psi = \begin{cases} -\frac{\pi}{5} r^2 \; R_1 < r < R_2 \\ -\frac{\pi}{5} R_1^2 \; r \leq R_1 \\ -\frac{\pi}{5} R_2^2 \; r \geq R_2. \end{cases} \tag{64}$$

~~$r = \sqrt{x^2 + y^2}$, and (x, y) are the coordinates of the grid-corner points. By differencing Ψ, the velocity components on the grid edges are obtained:~~

$$u = \frac{\Psi(i+1,j) - \Psi(i,j)}{\eta_x \Delta y}$$
$$v = -\frac{\Psi(i,j+1) - \Psi(i,j)}{\eta_y \Delta x} \tag{65}$$

~~Analogous to the 3-D case, $\eta_x \Delta y$ and $\eta_y \Delta x$ are the effective lengths of the cell edges normal in x-direction and y-direction, respectively. It can be easily shown that the resulting velocity field satisfies $\nabla \cdot \boldsymbol{u} = 0$. The initial concentration of the advected tracer is given by~~

$$c_0 = \frac{1}{2}\{[5(\phi - \frac{\pi}{3})] + [5(\frac{2\pi}{3} - \phi)]\}. \tag{66}$$

~~ϕ is the azimuth defined in a mathematically positive sense. One revolution of the tracer takes 5 s of simulation time, after which the analytical solution is identical to the initial state.~~

~~The case is simulated with increasing grid sizes of 50×50, 100×100, 200×200, 400×400 and 800×800, respectively. The integration step size is halved at each doubling of the resolution, starting at $\mathrm{d}t = 0.016\,\mathrm{s}$.~~
~~Figure 5a depicts the relevant hemisphere of the annulus with the solution after one revolution using the 800×800 grid. Figures 5b-f show the deviations from the exact solution on the different grids. Not unexpectedly, the largest error magnitudes occur towards the edges of the annulus, but generally diminish with increasing grid size. The respective error norms are shown in Table 1. L_∞ is the maximum error magnitude, which convergences with an average rate of $R_\infty = 0.8$. In contrast, Calhoun and LeVeque (2000) did not observe convergence in the L_∞ norm for the Péclet numer $Pe = \infty$ case. In the L_1 norm (mean absolute differences), the schemes accuracy is closer to second order with an average convergence rate $R_1 = 1.73$. The~~

~~convergence rate is not significantly affected by the order of accuracy of the reconstructions, which is 5^{th} by default. This suggests that the flux limiting has a profound impact on the results of this test case.~~

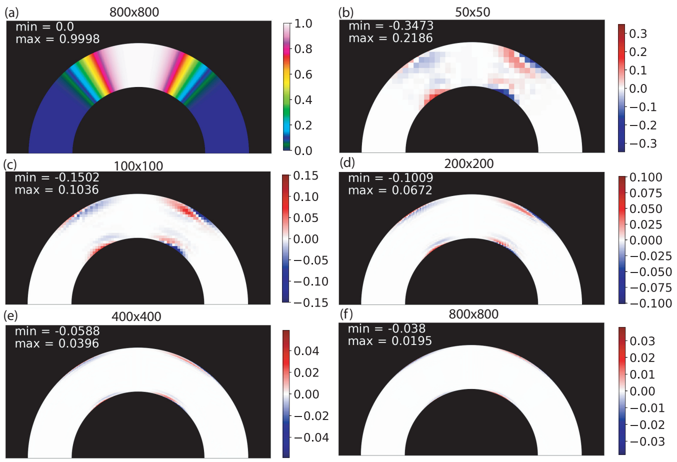

Figure 5. ~~Test tracer distribution in arbitrary units. (a): Solution after one revolution for a 800×800 grid. (b-f): Difference plots of difference between numerical and exact solution of the experimental convergence study for grid sizes 50×50, 100×100, 200×200, 400×400, and 800×800.~~

	~~50×50~~	~~100×100~~	~~200×200~~	~~400×400~~	~~800×800~~
~~L_1~~	~~3.194×10^{-3}~~	~~9.169×10^{-4}~~	~~3.079×10^{-4}~~	~~8.873×10^{-5}~~	~~2.607×10^{-5}~~
~~L_∞~~	~~0.3473~~	~~0.1502~~	~~0.1092~~	~~5.880×10^{-2}~~	~~3.800×10^{-2}~~
~~R_1~~	–	~~1.801~~	~~1.574~~	~~1.795~~	~~1.767~~
~~R_∞~~	–	~~1.209~~	~~0.574~~	~~0.779~~	~~0.630~~

Table 1. ~~Error norms L_1 and L_∞ and resulting rates of convergence R_1 and R_∞ for the different model grids in Fig. 5~~

3.2 Advection through an obstacle field

In t~~T~~his 2-D test, ~~initially consists of an approximation of a potential flow solution for an irregular obstacle field.~~ the computation domain contains randomly positioned circular obstacles of varying size. In a first step, an approximate potential flow solution is computed. Therefore, one step of the ~~explained~~ pressure projection method is applied on the initial wind field defined by $u = 1$ and $v = 0$. The resulting potential flow field is used to advect a test-tracer front, which is solely characterized by the left inflow boundary condition:

$$c = \begin{cases} 1 & t \le 40\,s \\ 0 & t > 40\,s \end{cases} \tag{67}$$

For the transversal-flow direction, periodic boundary conditions are used.

The reference simulation is carried out on a domain with 200×100 grid cells and a uniform grid spacing of $1\,\mathrm{m}$. The obstacle~~s are circular with~~ radii rang~~eing~~ from $5\,\mathrm{m}$ to $10\,\mathrm{m}$. The simulation is repeated on coarser grids with dimension sizes of 100×50, 50×25, and 25×13, respectively. Figure 6 shows the simulation results at $t = 150\,\mathrm{s}$. The obstacles are well resolved on the grid with $1\,\mathrm{m}$ spacing, but become more and more diffuse with decreasing grid resolution towards $8\,\mathrm{m}$ for the coarsest grid. The initially planar test-tracer wave is delayed and deformed by the obstacles. The qualitative impression is that the shape of the wave is not ~~really~~very sensitive to the grid resolution. Even in the most diffuse case, the position and shape of the wave matches that of the higher resolved simulations well. The wave dispersion can be quantified by considering the washout curves shown in Fig. 7, which are the spatially averaged concentrations at the outflow boundary versus time. For the case with the finest grid, the concentrations at the outflow boundary start to rise after $t = 145\,\mathrm{s}$ and peak at about $t = 185\,\mathrm{s}$. At $t = 250\,\mathrm{s}$, most of the wave is advected out of the domain. Remarkably, as already found by (Calhoun and LeVeque, 2000), the washout curve is not sensitive to the grid resolution up to $4\,\mathrm{m}$, which is at the transition when obstacles start to become diffuse. For the case with the coarsest resolution of $8\,\mathrm{m}$, the peak is slightly broader, peak concentrations are lower, and the peak occurs earlier by about $5\,\mathrm{s}$. At this grid resolution, the numerical diffusion of the advection scheme becomes important, as the resolution capability is around 6 grid points, which is barely enough to resolve the wave.

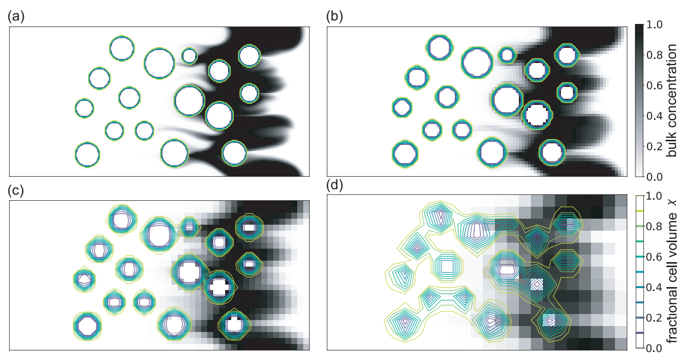

Figure 6. Results of the advection test with obstacles. Map plots of the concentration field of a test tracer after a simulation time of 150 s. The obstacles are drawn by contours of the volume-scaling field χ. Shown are the results of the flow simulations for the grids (a) 200×100 cells, (b) 100×50 cells, (c) 50×25 cells, and 25×13 cells , respectively.

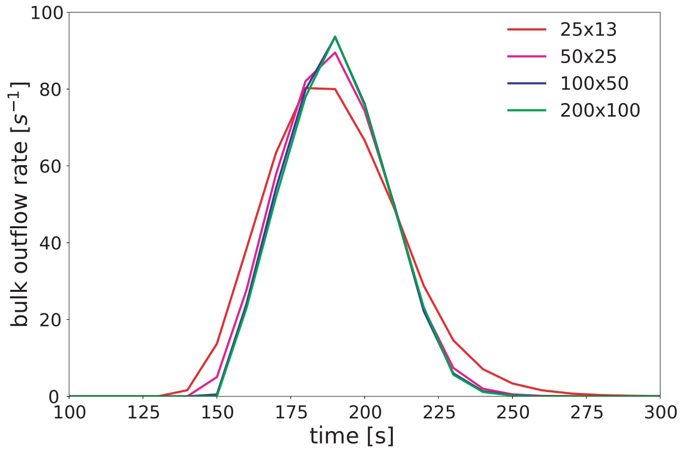

Figure 7. Washout curves of the test tracer for the different grid resolutions in Fig. 6. The values are computed by integrating over the modeled outflow at the downwind (right) domain border.

3.3 Rising thermal

In the rising thermal simulation described in Wicker and Skamarock (1998), the Euler equations without diffusion are solved on a 2-D domain with a height of 10 km and a width of 20 km. The grid spacing is uniformly 125 m. ~~Within the otherwise constant~~ The initially constant virtual potential temperature field of $\Theta_v = 300\,K$~~,~~ is perturbed by a circular thermal ~~perturbation is placed~~:

$$\Delta\Theta_v = \begin{cases} 2\cos^2\left(\frac{\pi r}{2L}\right) & r \leq L \\ 0 & r > L, \end{cases}$$
$$r = \sqrt{x^2 + (z - 2\,\mathrm{km})^2}, \qquad (68)$$
$$L = 2\,\mathrm{km}.$$

The initial vertical velocity is set to $w = 0\,\mathrm{m\,s^{-1}}$ and the horizontal velocity to $u = 20\,\mathrm{m\,s^{-1}}$. Periodic lateral boundary conditions are used and a rigid boundary is placed at the domain top. Due to buoyant forces, the thermal starts rising while it is constantly advected to the right and eventually re-enters the domain at the left boundary. ~~Finally, at the~~ After a simulation time of $t = 1000\,\mathrm{s}$, the thermal is again situated in the center of the domain.

Figure 9a shows the evolution of the thermal based on contours of Θ_v at the time steps $t = 0\,s$, $t = 350\,s$, $t = 650\,s$ and $t = 1000\,s$. Two distinct~~,~~ and symmetric rotors develop~~, and a~~. At the simulation time of $t = 1000\,s$, the overall appearance of the thermal matches well that of the original simulation by Wicker and Skamarock (1998) as can bee seen from the comparison with the original plot in Fig. 8. In our simulation, however, the thermal is more compact as it is confined between $x = \pm 2300\,\mathrm{m}$ and the peak height is at about $8100\,\mathrm{m}$. In the original simulation, it is confined between about $x = \pm 2600\,\mathrm{m}$ and below $8500\,\mathrm{m}$. Whether this slight discrepancy stems from the Boussinesq approximation or the different numerical schemes used can not be finally clarified. By scale analysis, the magnitude of the buoyant acceleration is about one or two orders less than that of the inertial acceleration in the given example. So, the Boussinesq approximation should indeed apply well in this example. The used 5^{th}-order upwind scheme is much less diffusive than the 3^{rd}-order scheme used by Wicker and Skamarock (1998). On the other hand, the flux limiting introduces ~~more~~ an adequate amount of diffusion ~~at~~ near sharp gradients to prevent oscillations and to ensure~~s~~ a positive solution ($\theta_v \geq 300\,\mathrm{K}$). This can explain our smoother contour lines inside the rotor. A slight asymmetry from the lateral advection can be noticed, which is most evident in the contours of vertical wind speed in Figure 9b. This asymmetry can be slightly more reduced by decreasing the integration step size (not shown). The combination of the advection scheme with the 3^{rd}-order SSP-RK3 time scheme gives stable results up to a Courant number of $C = 0.7$. Positivity of the solution is preserved up to $C = 0.5$.

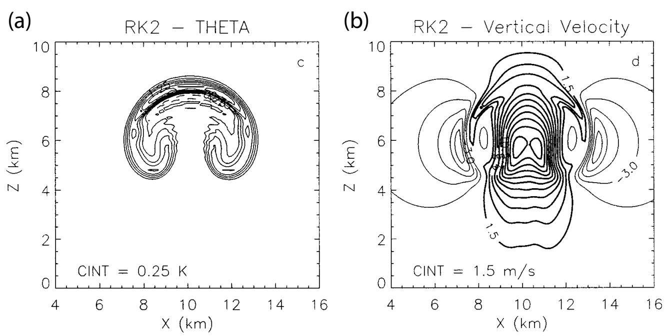

Figure 8. Original plot of Wicker and Skamarock (1998) (Figures 5c-d therein) ©American Meteorological Society. Used with permission. It shows the rising thermal problem computed using a third-order upwind scheme and a second-order Runge-Kutta scheme (Figures 5c-d therein): Shown are the potential temperature (a) and vertical velocity (b) after 1000 s of integration time.

3.4 Strong scalability test

We tested parallel scalability of the model for a domain spanning 350×350 grid cells in the horizontal dimensions and 82 grid cells in the vertical, thus consisting of approximately 10 million cells in total. For realistic demands on the pressure solver, a grid of diffuse buildings was placed at the bottom of the domain and vertical grid stretching was applied. The high-performance computing platform we used for the scaling test is organized into nodes, each one equipped with two 12-core Intel Xeon E5-2680 v3 CPUs, making in total 24 cores per node available. The strong scalability test is carried out for a variable number of cores ranging from one to 400. 400 cores correspond to a minimum average horizontal sub-domain size of 17.5 grid cells. Fig. 10 demonstrates the scaling efficiency of the model, as well as of the individual tasks for pressure projection

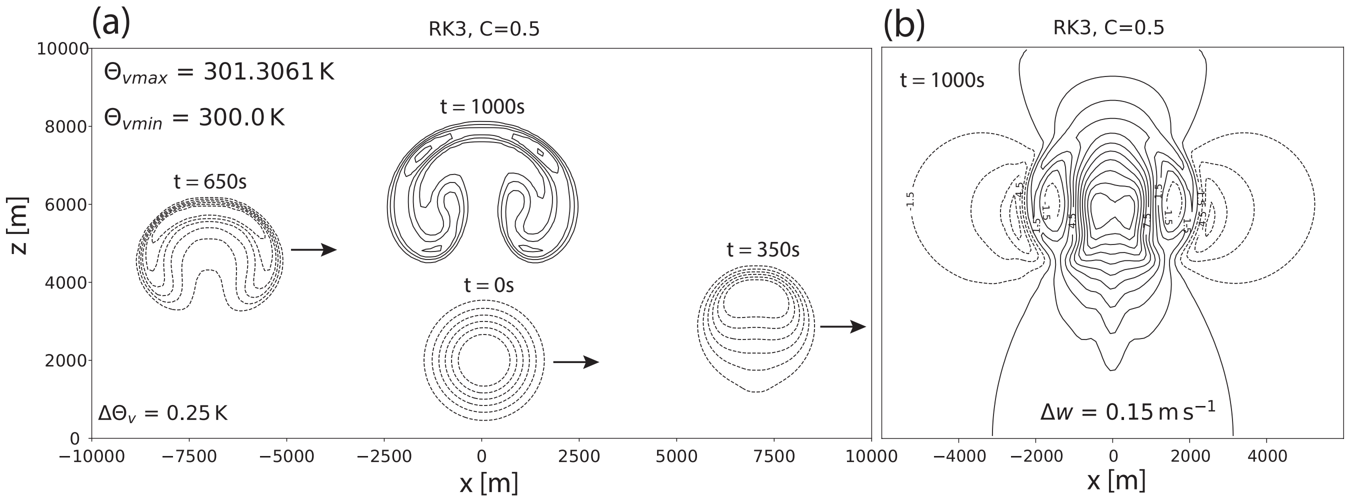

Figure 9. Rising thermal simulation with lateral advection: (a) Contours of virtual potential temperature at different time steps. The initial and intermediate states are drawn with dashed lines, the final state at $t = 1000\,s$ with solid lines. The contours with $\theta_v = 300\,\mathrm{K}$ are omitted. (b) Contours of vertical wind speed at $t = 1000\,s$. Dashed lines are used for negative values.

and advection computation of 3 momentum components and two scalars, which together are responsible for the bulk of the computation time. As a reference, the dashed lines show ideal scaling starting from a reference of one single core. Comparing the experimentally obtained curves with the idealized curves, firstly, a peculiar drop in scaling efficiency between 4 and 9 cores can be noticed. However, this drop cannot be explained by the parallelization design and it was also not observed using a different platform with less cores (not shown). The arithmetic-intense advection computation shows, apart from the already noted drop between 4 and 9 cores, excellent scaling, which becomes even super-linear above 100 cores due to cache effects. Not surprisingly, the pressure solver, which requires two communications for each smoothing iteration, does not scale so well. While cache effects can balance the increasing communication overhead up to 200 cores, above this number, scaling is no longer satisfactory. Due to the lower costs of the pressure solution in comparison with the advection computation, the model shows a very good scaling up to 400 cores for this test case. Note, however, that the best decomposition to benefit from cache effects shifts toward a lower number of cores when the vertical dimension size is decreased. In theory, the implementation of the smoothing procedure supports overlapped communication and computation, as the matrix-vector product of the halo layer is computed independently from the inner matrix-vector product. In this test, we could not observe any true overlap, which would require further investigation. Addressing this feature in future can help to additionally improve scalability of the pressure solver.

4 ~~Michelstadt wind-tunnel experiment~~ Model evaluation with wind-tunnel experiment and grid size sensitivity tests

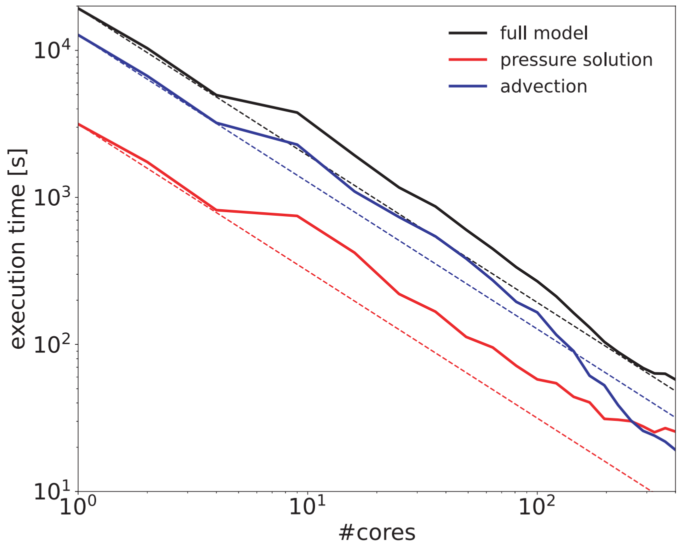

Figure 10. Strong scalability of CAIRDIO v1.0 tested for a domain with $350 \times 350 \times 82$ grid cells using 1 to 400 cores on a high-performance computing platform. Dashed lines show ideal scaling.

The wind tunnel experiment "Michelstadt", which was carried out in the wind tunnel WOTAN (Lee et al., 2009) of the University of Hamburg, Germany, is used to evaluate the model accuracy and reliability ~~against a physically based dataset~~ of dispersion simulations within an urban canopy. ~~The benefits of using~~ Advantages of wind tunnel-data over field observations ~~for numerical model evaluation~~ are the accurately controlled ~~and determined~~ approaching-flow conditions~~,~~ and the high density of wind and concentration measurements in both space and time ~~the high spatial and temporal resolution of measurements, and the~~ , which results in a high statistical significance of the data~~compared to field data~~(Schatzmann et al., 2017). ~~Assuming the validity of the scale invariance, wind-tunnel experiments provide a reliable basis of comparison under idealized conditions (e.g. neutral stratification, absent surface fluxes, temporally constant and horizontally homogeneous approach-flow statistics).~~

The fictitious city district "Michelstadt" is ~~the name of a fictitious model city district, designed at an assumed~~ based on a typical Central European downtown area with spacious polygonal courtyards surrounded by residential building units at a scale of 1:225 (see Fig. 11a). ~~The district spans an area of roughly $1350\,\mathrm{m} \times 850\,\mathrm{m}$ at the full scale. The simplified geometry is based on a typical Central European downtown area, with spacious polygonal courtyards surrounded by residential building units. The orientation and length of street-canyon sections are highly variable, and isolated squares are present. All~~ Building roofs are approximated by ~~a flat~~ horizontal surfaces ~~(flat-roof model)~~, and their ~~full-scale~~ heights range from $15\,\mathrm{m}$ to $25\,\mathrm{m}$ at the full scale. ~~See Fig. 11a for an overview of the building layout.~~

The approaching ~~wind field is~~ flow can be characterized by a neutrally stratified and horizontally homogeneous urban boundary-layer ~~flow with neutral stratification. The~~ with a parametric surface-roughness length ~~is comparatively large with~~ of approximately $1.4\,\mathrm{m}$.~~, implying the seamless incorporation of the test section into a more extensive urban area. Turbulence of the approaching flow is initiated by an arrangement of vertical spikes, and the passage of the flow over an extended pattern of surface-roughness elements establishes turbulent kinetic equilibrium in the wind-tunnel experiment. In order to characterize the statistical properties of the approaching flow more accurately, experiments were carried out where the entire wind-tunnel floor was covered with roughness elements. The actual e~~Experiments ~~with the model city~~ were carried out using two different ~~wind directions of the~~ approach-flow directions of ~~(~~$0\,°$~~,~~ and 180~~),~~.~~, where the reverse 180° direction can be used to verify the robustness of model results after parameter tuning with the reference case 0°.~~ This provides the opportunity to test the robustness of model results after model-parameter tuning using the wind-tunnel results from the default $0\,°$direction. The experimental datasets consist of time-resolved flow and dispersion measurements, from which ~~also the stationary~~ temporally averaged statistics were calculated. A dense array of sensors ~~covers~~ provided horizontal wind measurements within planes at heights of $2\,\mathrm{m}$, $9\,\mathrm{m}$, $18\,\mathrm{m}$, $27\,\mathrm{m}$, and $30\,\mathrm{m}$ over a restricted area.

For the dispersion modeling, neutral-buoyant gas was released at different locations on the floor (see Fig. 11 for the locations of the release points). Release points S2 and S4 were used for the approach-flow direction of $0\,°$, S6, S7 and S8 for the reverse direction. S5 was used for both wind directions. ~~Depending on the tested scenario (fast response vs. average air pollution), the releases were in puffs or continuous. The concentrations, converted to dimensionless units of ppmv, were measured using flame-ionization detectors all placed~~ Tracer-gas detectors to measure concentrations were all positioned at a full-scale height of $7.5\,\mathrm{m}$ and at different horizontal positions depending on the source. Further information on the experiment and the datasets are provided in Baumann-Stanzer et al. (2015).

The numerical simulations are performed at the full scale using a series of grids with horizontal resolutions of $5\,\mathrm{m}$, $10\,\mathrm{m}$, $20\,\mathrm{m}$, $40\,\mathrm{m}$, and $80\,\mathrm{m}$. The $5\,\mathrm{m}$ resolution is used as ~~for~~ the reference.~~, and t~~The coarser domains are used to test the grid-sensitivity of the dispersion simulation~~ to the spatial resolution~~. The vertical grid spacing near the surface ranges from $2\,\mathrm{m}$ for the finest grid to $7\,\mathrm{m}$ for the coarsest ones.~~, and~~ It is increasingly stretched beyond $30\,\mathrm{m}$ above surface. The effective domain height is approximately $600\,\mathrm{m}$, which corresponds to the scaled wind-tunnel height. Above this height, the wind components are dampened to the horizontally and temporally average state.

A first precursor simulation is run with periodic boundary conditions to obtain laminar and turbulent inflow profiles for the full vertical domain extend. These are used to drive the actual experimental simulations containing the buildings and test-tracer release points. In this precursor simulation, which uses a shorter domain ~~with a total~~ length of ~~about only~~ roughly $1\,\mathrm{km}$, buildings are not present and the entire rigid bottom-domain boundary is covered with roughness elements.~~, with t~~ The geometries and arrangement of elements are adapted from the experiment. In order to model the effect of the lateral wind-tunnel confinement, rigid walls are placed at the flow-perpendicular boundaries. The modeled statistics of the established neutrally-stratified boundary layer flow are re-scaled to the reference wind speed of $6\,\mathrm{m\,s^{-1}}$ at $50\,\mathrm{m}$ height. The obtained horizontally averaged vertical profiles are vertically interpolated for the coarse-grid simulations. In the experimental simulations containing the model city, turbulent approach-flow conditions with the correct target intensities are generated using the turbulence-recycling scheme. The recycling plane is placed well downstream of the model city and after a short pattern of roughness elements near the outflow boundary (Fig. 11a). This allows the application of a much shorter additional domain fetch for turbulence ~~recycling,~~generations.

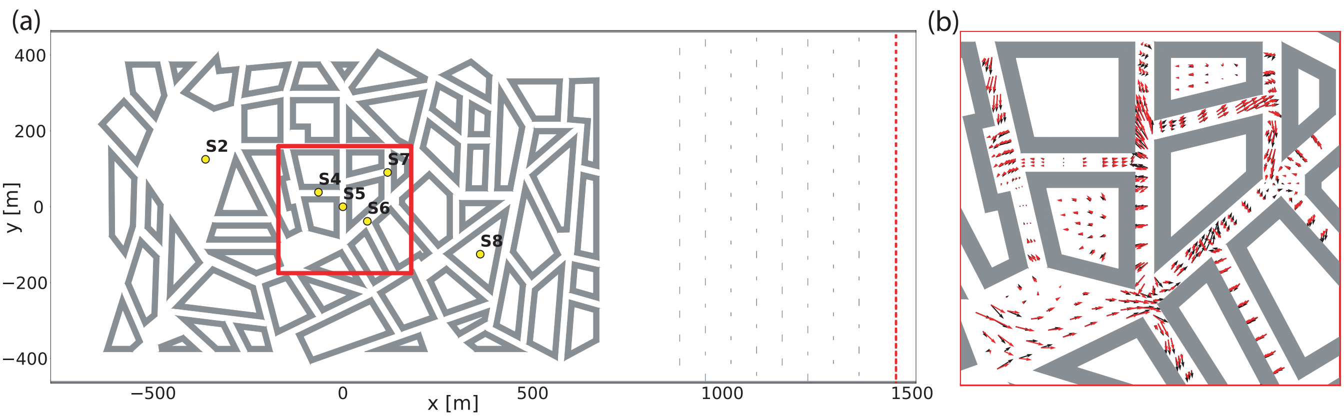

Figure 11. (a) Depiction of the model domain for the numerical simulation of the wind tunnel experiment "Michelstadt". Rigid boundaries, including the buildings, the side walls and the roughness elements are drawn using grey color. The yellow circles mark the tracer-gas release points. The red dotted line is at the position of the turbulence recycling plane. The area within the red bounding box contains the horizontal wind measurements arranged in horizontal planes. (b) Comparison of measured (black arrows) and modeled (red arrows) time-averaged horizontal wind vectors at $2\,\mathrm{m}$ height.

~~as the total recycling fetch can be much larger using the upstream domain.~~ This particular positioning of the recycling plane ~~can be justified~~ is also well supported by the similar parametric roughness length of the elements and the model city. ~~Apart from that~~Also, the extracted fluctuation intensities are ~~always~~ re-scaled to the values of the target wind field, which further reduces the impact of obstacles further upstream.

4.1 Inflow profile

Figure 12 shows the modeled and re-scaled horizontally averaged statistics of the boundary-layer flow ~~using~~ generated by the precursor ~~periodic domain~~ simulation. The experimentally obtained profiles are included for comparison. In the modeled mean horizontal wind speed, the roughness layer extends up to $20\,\mathrm{m}$ ~~above ground~~ height, ~~and~~ above which it is proceeded by the logarithmic Prandtl layer. The slope of the modeled wind profile in the semi-logarithmic depiction matches the observed profile well. The modeled turbulent intensities are generally ~~too low~~ underestimated by up to $20\,\%$ when compared ~~to~~ with the observations~~ed ones~~. ~~Partly this can be attributed to the neglected subgrid and numerical diffusion.~~ This difference is most likely due to artificial dissipation in the model. ~~Apart from that, t~~The peak values at about $400\,\mathrm{m}$ height are probably residual reflections ~~from~~ at the domain top, which are not ~~fully~~ completely ~~captured~~ prevented by the dampening. The measurements below a height of $20\,\mathrm{m}$ are more difficult to compare, since they are located within the roughness layer~~, and their values~~ and thus are strongly ~~depend on~~ influenced by the relative location to the nearby roughness elements.

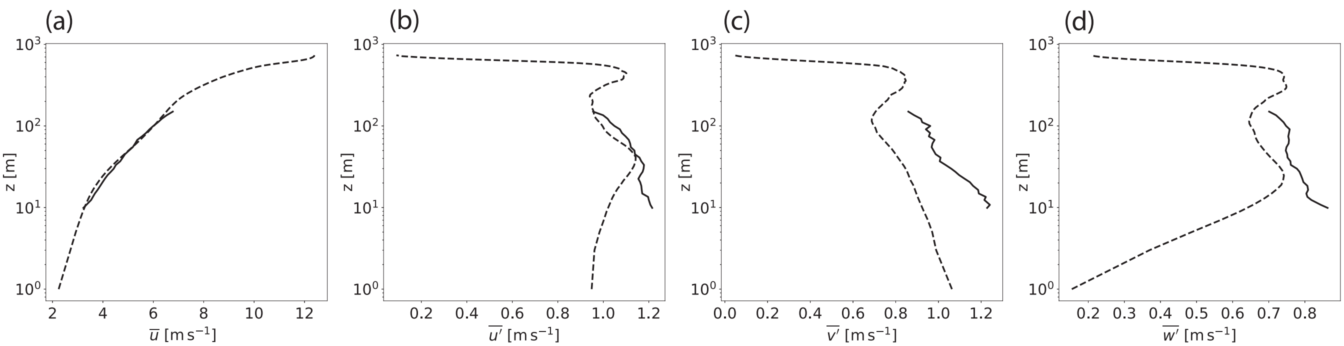

Figure 12. Modeled (dotted lines) and measured (full lines) mean and turbulent statistics of the approach flow in the "Michelstadt" wind tunnel experiment. Depicted are (a) the temporal mean velocity component $\overline{u}$ and (b-d) the grid-scale turbulent intensities $\overline{u'}$, $\overline{v'}$, and $\overline{w'}$, respectively.

4.2 Horizontal wind evaluation

The modeled horizontal wind is evaluated on the reference grid with $5\,\mathrm{m}$ horizontal resolution. Figure 11b) gives a first qualitative impression of the agreement~~, as i~~. It shows the time-averaged horizontal wind vectors both for the model and the measurements within the plane of $2\,\mathrm{m}$ height. Overall, the model is capable of reproducing the measured flow pattern. However, the modeled wind direction does not always match the corresponding measured vector well, which is most notably near some intersections. The scatter plots for wind speed (Fig. 13) and wind direction (Fig. 14) give a more quantitative and conclusive picture. The accuracy of modeled wind speed is high~~, when~~ taking the normalized mean standard error (NMSE) as a proxy~~,~~ ~~whose~~ . Its value is consistently below 0.1. The fractional bias (FB) shows only a very slight underestimation of wind speed~~s~~ (0.02 - 0.07). This is not very surprising, ~~since~~ as the model resolution of $5\,\mathrm{m}$ is not high enough to ~~fully~~ completely resolve the ~~small-scale~~ re-circulation~~s~~ zones within the urban canopy (Xie and Castro, 2006). Thus, the modeled wind speed within circulation zones tends to be lower as a result of more extensive spatial averaging.

4.3 Dispersion ~~simulation~~ evaluation

~~The dispersion of point-source emissions is evaluated in the continuously emitting mode.~~ The resulting time-averaged modeled concentrations are interpolated to the detector si~~d~~tes and paired with corresponding measurements. As proxy for the quality of model results in comparison to the measurements, ~~the normalized mean standard error (~~NMSE~~)~~, ~~the fractional bias (~~FB~~)~~ and additionally the fraction of within factor 2 (FAC2) are calculated. Based on the guidelines presented in ~~Baumann-Stanzer et al. (2015)~~ Hanna and Chang (2012), acceptance criteria for a valid simulation are NMSE < 6, $|\mathrm{FB}| < 0.67$ and FAC2 > 0.3.
The simulations with the approach flow direction of $0\,°$are used to optimize the model configuration with respect to these test criteria, while the reverse flow direction is used to validate the robustness of model results using the same parameter configuration. One important model tuning parameter ~~for example~~ is the Smagorinky constant, which was set to $c_s = 0.15$ for all

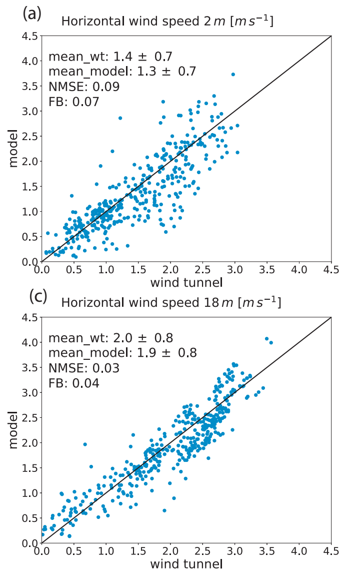

Figure 13. Scatter plot of modeled vs. measured horizontal wind speed within planes at different heights. For a quantitative comparison, NMSE and FB are calculated.

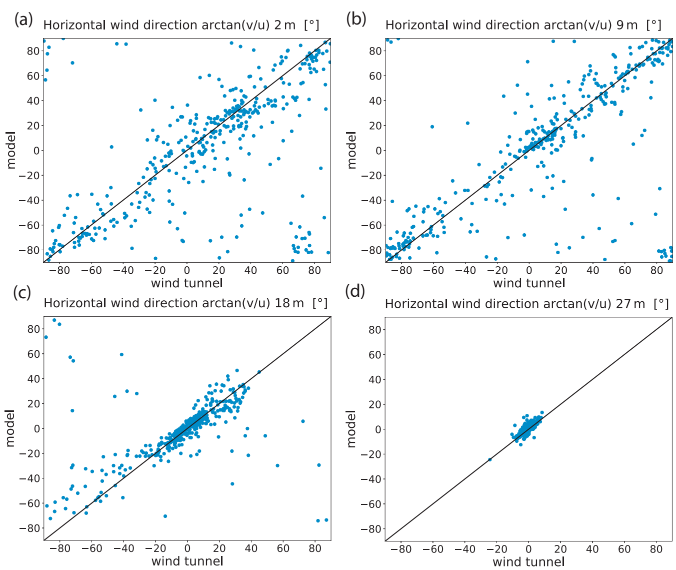

Figure 14. Scatter plot of modeled vs. measured horizontal wind direction within planes at different heights.

simulations. However, for the simulations with $40\,\mathrm{m}$ and $80\,\mathrm{m}$ resolution, the vertical mixing length ~~was~~ had to be increased to $20\,\mathrm{m}$ within the urban canopy to ~~balance~~ compensate for the ~~underrepresented building-induced~~ poorly defined eddies important for vertical mixing~~ at such coarse resolutions~~.

Among the tested sources, S2 is the only one emitting into an ~~quite~~ open area, whereas all other sources are placed within street canyons or courtyards. Thus, S2 is probably the least difficult to simulate. Figure 15 gives an impression of the simulated time-averaged plumes resulting from S2 at the height of detector~~s~~ sites. Figure 15a) shows the reference simulation with the highest grid resolution. The overall qualitative agreement with measurements seems very good, except for a street canyon in roughly -45 °direction and in close proximity to the source~~, wherein~~ . Therein, the modeled concentrations are too low. ~~Not surprisingly~~ Expectedly, increasing the grid spacing results in a deterioration of the qualitative agreement with measurements and with the reference simulation. For example, increasingly less tracer gas is advected inside the flow-parallel street canyon, where most of the detectors reside. Instead ~~of~~, the plumes ~~become~~ are increasingly smeared over a wider area. This is especially evident ~~at~~ for the $20\,\mathrm{m}$ grid spacing, whereas ~~at~~ for the even coarser resolutions of $40\,\mathrm{m}$, the agreement with measurements improves again. Notably, ~~T~~this behaviour is only observed for this particular source. The grid resolution of $80\,\mathrm{m}$ clearly shows the least accurate results. While the dispersion pattern still resembles those of the better resolved simulations and shows the imprint of buildings, concentrations are too high in the down-wind swath. At this resolution, ~~dynamics induced by buildings and important for vertical mixing cannot be properly represented anymore.~~ a more elaborated mixing parameterization could still give improved results over the simple Smagorinsky model.

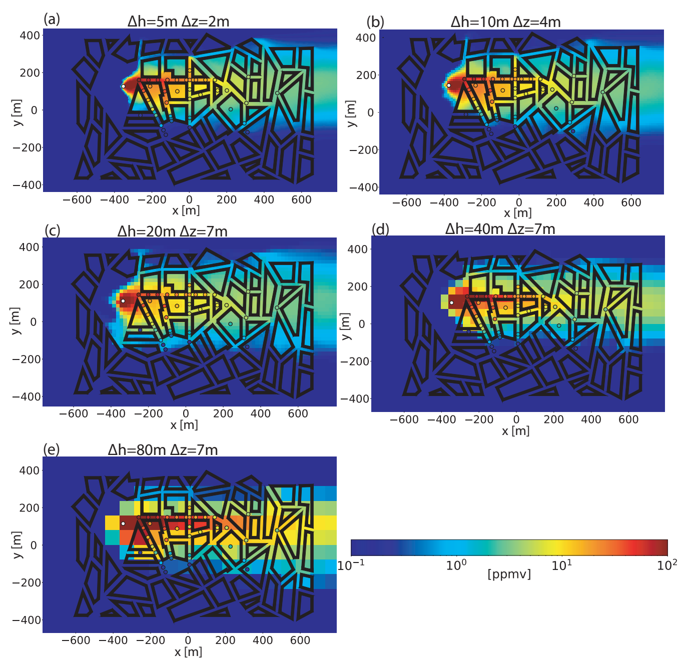

Figure 15. Map plots of modeled concentration fields in ppmv at $7.5\,\mathrm{m}$ height for source S2 and different grid resolutions. The black circles mark the location of measurements for this particular source, and the fill color indicates the measured concentration according to the color bar of the map plots.

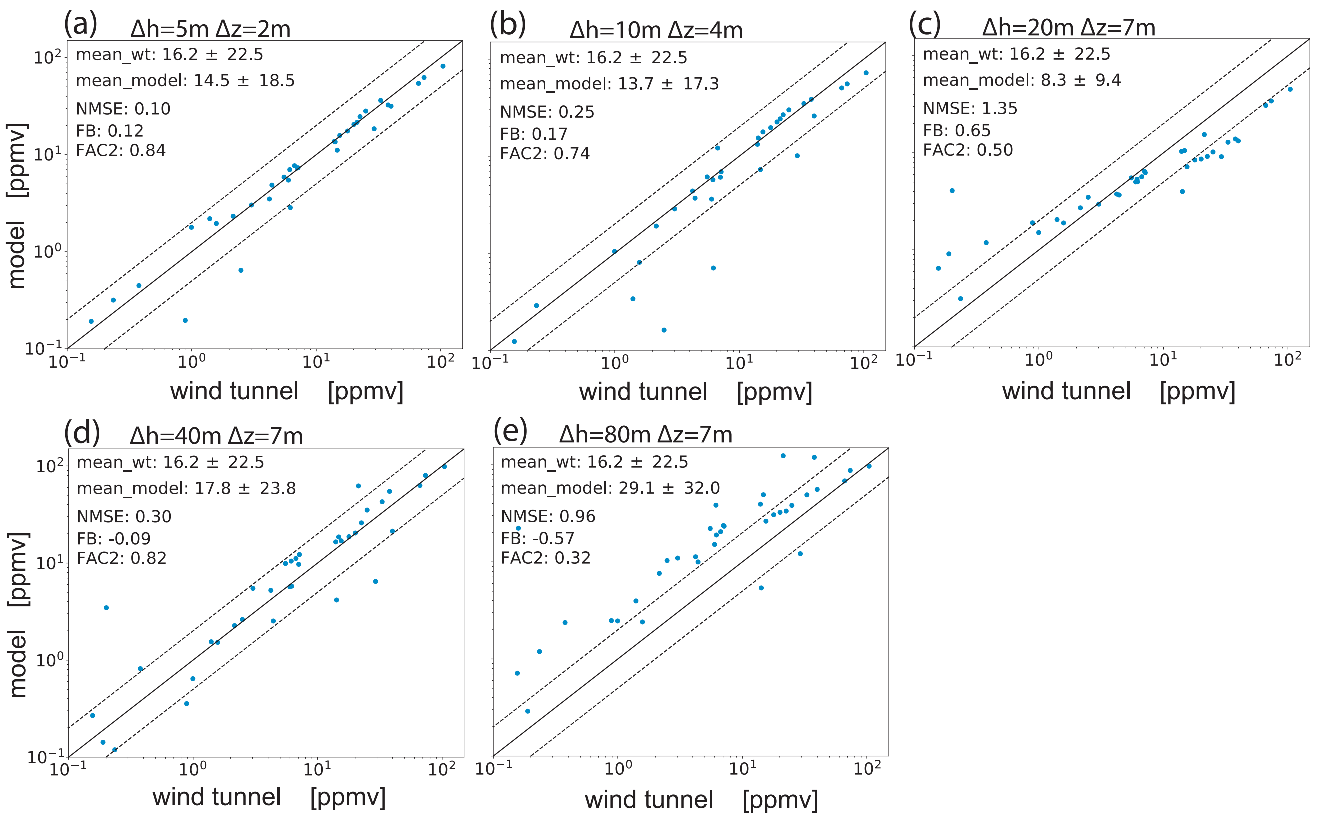

Figure 16. Scatter plots of measured vs. modeled concentrations for source S2 and different grid resolutions. The dotted lines confine the region within a factor of two of measurements.

For the quantitative evaluation of the presented simulations, ~~the paired data is presented as~~ modeled and measured values are compared in scatter plots in Fig. 16, and the aforementioned statistical acceptance parameters are derived. For the reference case, most of the model data is tightly distributed near the bisecting line. In fact, the model accuracy is very good ($\mathrm{NMSE} = 0.10$), with only a slight positive bias toward too low values ($\mathrm{FB} = 0.12$) and only few outliers present ($\mathrm{FAC2} = 0.84$). The decrease in model accuracy with increasing grid spacing is evident in the scatter plots, as modeled values tend to be too low for high concentrations measured and visce versa ~~, respectively~~. This results in a steady increase in $\mathrm{NMSE} = 0.25$ for the $10\,\mathrm{m}$ grid spacing and $\mathrm{NMSE} = 1.35$ for the $20\,\mathrm{m}$ grid spacing. Since FB is more sensitive to deviations at the upper end of the logarithmic scale, the smearing also results in an increasingly positive bias ($\mathrm{FB} = 0.17$ and $\mathrm{FB} = 0.65$). The trend is, however, reversed at the even coarser resolution of $40\,\mathrm{m}$, resulting in an improvement of model results for this particular source. Finally, the $80\,\mathrm{m}$ case shows a large negative bias ($\mathrm{FB} = -0.57$) and a value of $\mathrm{FAC2} = 0.32$ at the verge of acceptance. Table A1 summarizes the statistical parameters for all other cases simulated.~~ Based on it~~From the sensitivity results in Tab. A1, it can be concluded that ~~while moving to ever coarser grid resolutions~~ the quality of model results generally declines with decreased

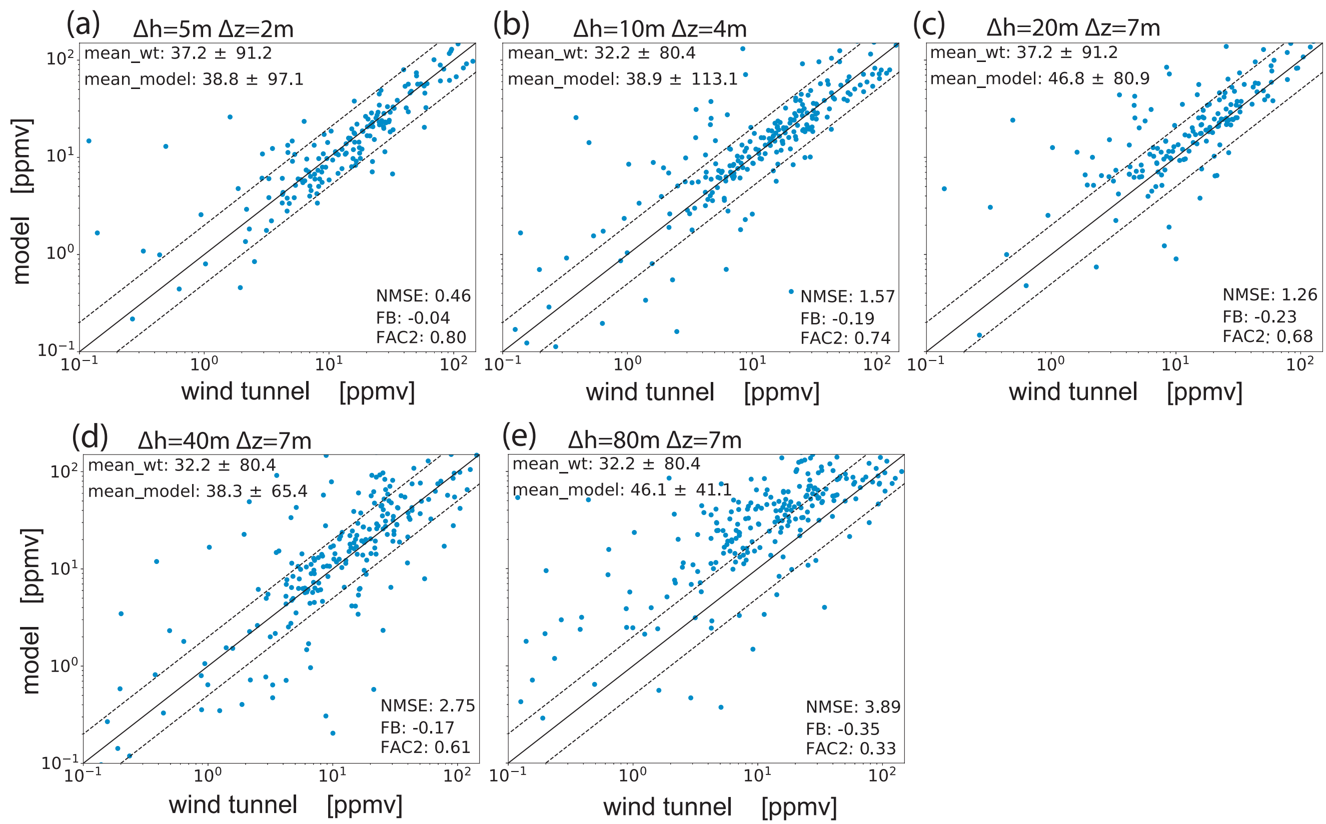

Figure 17. Scatter plots of measured vs. modeled concentrations combined for all sources and different grid resolutions. The dotted lines confine the region within a factor of two of measurements.

grid resolution (mostly evident in NMSE value), but not to an extend to compromise model reliability at $40\,\mathrm{m}$ resolution, where buildings are represented diffusely. Only one source located within a courtyard proofed to be more problematic ~~at~~ with $40\,\mathrm{m}$ grid spacing, as the resulting plume was not well contained within. We attributed this ~~which is due~~ to the difficulty in ~~modeling~~ representing diagonally orientated building walls as impermeable as they are at such coarse resolutions. Using the $80\,\mathrm{m}$ grid, the model still performs acceptable for some of the sources. Figure 17 shows scatter plots of ~~the data pairs~~ modeled and observed data collected from all simulated cases with a given resolution~~, whose~~ . The according statistical results are again summarized in Table~~.~~ A2. It is shown~~s how~~ that the reliability of model results is not very sensitive to the grid spacing down to $40\,\mathrm{m}$ resolution. For example, FAC2 decreases from a value of 0.8 at $5\,\mathrm{m}$ to 0.61 at $40\,\mathrm{m}$ grid spacing. Conversely, NMSE increases from 0.54 to 2.75, which is still well within the acceptable range. The average fractional bias is below $\mathrm{FB} = 0.2$ for all simulations, except for the $80\,\mathrm{m}$ case, where it is much larger ($\mathrm{FB} = -0.35$). In this regard, the increased vertical mixing length showed to be an effective tuning option in combination with the $40\,\mathrm{m}$ resolution to keep the bias comparatively low

(FB $= -0.17$). It has to be kept in mind that this test uses isolated point sources. When applied to a more realistic scenario with traffic emissions, modeled for example by emission lines, it can be hypothesized that scattering of the data would be of less concern, ~~since~~ because the pollution is more widely distributed horizontally. Therefore, ultimately, the most important reliability measure in our view is the FB value, as it is a proxy whether the model will under- or over-estimates air pollution. In this regard, the $80\,\mathrm{m}$ resolution is the least accurate, and it is currently not aspired without the use of a more sophisticated mixing parameterization. Finally, when comparing all model results with only those from the $180\,°$-approach flow tests ~~only~~ using the same parameter configuration, it was found that ~~this~~ these latter ~~test~~ cases ~~with the model parameters adopted from the $0\,°$-approach flow runs proofed to be~~ could be modeled not significantly less ~~reliable~~ accurately. This is largely attributed to the simplicity of the model, as it requires little ~~free~~ parameter tuning.

4.4 ~~Urban area within idealized basin~~

~~In this simulation, additional model features are combined for a more realistic test case, compared to the previous ones. For simplicity, this test is quasi 2-D. The third dimension is needed only for a realistic 3-D turbulent mixing, as turbulent mixing behaves fundamentally different using two dimensions only.~~

~~The domain spans $2880\,\mathrm{m}$ in the lateral direction (x-dimension), $640\,\mathrm{m}$ in the streamwise direction (y-dimension) and $840\,\mathrm{m}$ in the vertical one (z-dimension). The horizontal grid spacing is $20\,\mathrm{m}$ and grid stretching is applied in the vertical dimension. The grid spacing for the lower most levels is $7\,\mathrm{m}$, and is increased beyond with approaching $50\,\mathrm{m}$ for the upper most levels. An urban area represented by rectangular buildings is placed at the bottom of an idealized basin whose cross-section is modelled by the following analytic expression for the terrain-height function:~~

$$\cancel{h(x) = -\Delta h \exp\left(-\frac{|x|^3}{L^3}\right)} \qquad (69)$$

$$\cancel{L = 1\,\mathrm{km}}$$

$$\cancel{\Delta h = 200\,\mathrm{m}}$$

~~The terrain-height function is constant in the streamwise direction, and also the building pattern is repeated in this direction. For all rigid boundaries, including the diffusely discretized buildings, a surface roughness length of $z_0 = 0.1\,\mathrm{m}$ is assumed. The initially neutral stratification of the atmosphere ($\Theta_v = 280\,\mathrm{K}$) is forced towards stable or unstable conditions by prescribing a constant surface temperature, which, in relation to the initial state of the atmosphere, is cooler or warmer by $5\,\mathrm{K}$. For the heating case, also vertical building walls and roofs have an increased surface temperature, whereas for the cooling case, their temperature is kept at $\Theta_v = 280\,\mathrm{K}$. The wind field is initialized with an uniformly constant horizontal wind speed of $v = 1\,\mathrm{m\,s^{-1}}$ blowing through the valley. Periodic lateral boundary conditions are used for the y-dimension, and radiation boundary conditions for the x-dimension. A Rayleigh damping layer relaxes the state variables u, v, w and Θ_v at the domain top. An area source of a test tracer, which emits at a rate of $1\,\mathrm{u\,s^{-1}}$, is placed at the ground near and between the buildings, mimicking traffic emissions. The boundary conditions for the test tracer are homogeneous-zero Dirichlet on all sides, preventing a re-entrance of the plume on the upstream domain boundary. For the cooling-case the model was integrated for 18 h after which~~

~~an inversion layer was well established. For the heating case, after an integration time of 6 h, no further development of the flow and dispersion pattern occurred.~~

~~Figure 18 shows maps of Θ_v and the tracer concentration fields for both the convective and stable case at the instantaneous times of 6 h and 18 h, respectively. The fields are averaged along the y-dimension to depict the basin cross section. In the convective case, 4 pronounced rotors are symmetrically aligned across the basin, with three main near-surface convergence zones: One located directly over the city, and the remaining two on the basin edges. Heat transfer is locally enhanced either by higher surface wind speeds over the basin slopes or through the additional surface area of the buildings within the city. As a result, a pronounced heat island can be observed over the city, which is responsible for the lifting of the air pollution plume originated from the city inside the strong updraught. The air pollution eventually mixes throughout the height range of the simulated boundary layer. Near-surface air pollution in the city remains comparatively low and concentration gradients are weak. In the stable case, only a shallow boundary layer develops. However, the basin is filled with cooler air and a pronounced inversion layer is present. Below the inversion layer, an erratic shallow circulation pattern with weak horizontal winds is present. Also noticeable are weak katabatic winds blowing down-slope towards the city, where the coldest air gathers. The inversion layer keeps air pollution trapped, and therefore the concentrations increase with advancing simulation time. This phenomenon of increased air pollution inside city basins is commonly observed during winterly high-pressure periods. While the air pollution within the basin is distributed evenly horizontally it decreases with height, the highest concentration being present at street level in the city.~~

~~In this example, it is demonstrated that the effects of a wavy surface orography interact in a complex way with the thermal effects resulting from surface-heat transfer. This is especially true for the convective case, where both the urban heat island effect and the lee effect of the slope have a large influence on the location of the zones of convergence. In any case, the incorporation of terrain effects from the surroundings is crucial for other more accurate dispersion simulation, which highlights the importance of a holistic simulation approach. From a numerical point of view, the use of a curve-linear grid is advantageous over a standard Cartesian approach, as the vertical grid stretching can be applied just in the same way as for a flat domain. This results in a much lower number of grid boxes for the same near-surface resolution.~~

5 Summary

In this paper, ~~a~~ the new large-eddy simulation-based ~~modeling approach~~ model CAIRDIO for ~~urban application~~ urban dispersion simulations was presented. In this paper, a new large-eddy based dispersion modeling approach for urban application was presented. The model uses diffus~~iv~~e obstacle boundaries in the framework of a finite volume discretization to represent building walls at a wide range of spatial resolutions. Diffus~~iv~~e obstacle boundaries allow for a consistent implementation of buildings in the model code, as they are essentially described by a scalar field for the volume-scaling factors and a vector field for the area-scaling factors. Using these fields to discretize the differential operators, boundary conditions are incorporated ~~naturally~~ automatically and the governing equations are solved for the entire computation grid without ~~requiring to discern~~ the need to distinguish different types of grid cells. This ~~permits~~ allows for a straightforward and vectorized implementation of spatial

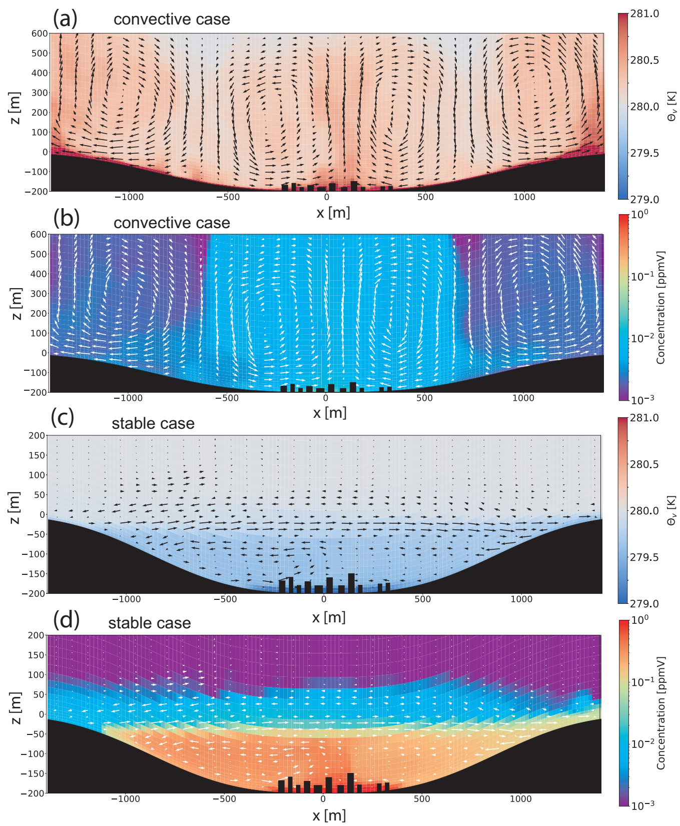

Figure 18. ~~Model results of the idealized urban dispersion simulation averaged along the y-axis at 6 h simulation time (convective case) and 18 h simulation time (stable case). The panels (a) and (c) show the virtual potential temperature for a warmer and a cooler surface, which results in an unstable and stable stratification, respectively. Panels (b) and (d) show the implications on air pollution dispersion. To better display the cross-stream circulation pattern in the stable case, only the lower part of the domain is shown and the wind vectors are magnified 10-fold compared to those of the convective case.~~

operations. The inherent option for under-resolved diffusive buildings enables the model to be applied at marginal grid resolutions inaccessible for conventional Cartesian-grid models. The computational savings can be invested in larger domains to model whole cit~~yies~~ areas and ~~its~~ their surroundings. The large-scale influence of orographic terrain ~~influence~~ can be ~~efficiently~~ adequately represented by curve-linear grids. To benefit from modern hardware architecture, the model is parallelized using a 2D-domain decomposition method, which is sufficient for the expected large grid-aspect ratios of typical boundary-layer applications. The numerical schemes ~~used~~ presented are approved and efficient choices. Linear upwind schemes of selectable order of accuracy with optional limiting are used for advection, a static Smagorinsky model for subgrid turbulence modeling, and multi-stage higher-order time methods for model integration. The coupling with the mesoscale meteorology can be obtained through different forcing methods using data from a mesoscale host model. ~~A 2-D advection test with a known analytic~~

~~solution revealed that the spatial accuracy of the scheme is in the expected range of the design. The sensitivity study with the~~ A simple numerical test, consisting of a test-tracer being advected~~ion~~ by a potential-flow through an obstacle field, demonstrated the robustness of the obstacle discretization up to grid spacings where the resolution capability of the numerical schemes start to interfere. The ~~model~~ results of the rising thermal experiment to test the dynamic core are plausible and similar to those presented in the original studies. ~~The advantages of the model design were demonstrated, in particular the diffusive obstacle treatment. When compared to~~ Finally, we evaluated the model with data ~~of~~ from the "Michelstadt" wind tunnel experiment.~~,~~ In this study, the model ~~simulated~~ reproduced reliably the complex wind fields and embedded tracer dispersion. ~~As a result~~ For the latter application, this was also true ~~even for~~ using spatial resolutions beyond $20\,\mathrm{m}$, at which buildings can only be represented as increasingly diffuse features.~~, t~~The sensitivity study researching grid-spacing of the dispersion test showed promising results for a future study with more realistic emission distributions and real~~-mid~~-sizes cities. In near future, also the coupling with mesoscale meteorology will be addressed. From previous and accompanying air-quality studies, simulations with the regional CTM COSMO-MUSCAT are available for different German cities, including Berlin and Leipzig, for which also comprehensive measurement data are available for model evaluation. In this framework, a promising application could be a more comprehensive and holistic model evaluation with field data, as ~~additionally to airy monitoring,~~ mobile measurements ~~may become~~ are available for the city of Leipzig in addition to operational air monitoring. Potential model improvements worth ~~addressing~~ to be addressed in the future are the parameterization of air pollution sinks and the implementation of a simple urban atmospheric chemistry. Alternatively, it would be interesting to include diffusive obstacle boundaries in the aerosol-chemistry code MUSCAT, and to investigate whether there is a benefit ~~in~~ for the application on urban air pollution modeling.

Code and data availability. The source code of CAIRDIO model version 1.0, utilities for pre- and postprocessing, as well as evaluation data are accessible in release under the license GPL v3 and later at https://doi.org/10.5281/zenodo.4159497 (Weger et al., 2020).

Author contributions. Michael Weger contributed in model development, implementation, evaluation, and paper writing. Oswald Knoth and Bernd Heinold assisted in model development, paper writing and proof reading.

Competing interests. All authors declare that they have no competing interests.

Acknowledgements. Wind tunnel data of the "Michelstadt" case were kindly provided by Bernd Leitl and Frank Harms from the Meteorological Institute, University of Hamburg, Germany. The authors gratefully acknowledge the Centre for Information Service and High Performance Computing (Zentrum für Informationsdienste und Hochleistungsrechnen, ZIH) TU Dresden for computing time and their service.

Appendix A

source (Δh)	mean wt [ppmv]	mean model [ppmv]	NMSE	FB	FAC2
0° approach flow					
S2 (5 m)	16.2 ±22.5	14.5 ±18.5	0.10	0.12	0.84
S2 (10 m)	16.2 ±22.5	13.7 ±17.3	0.25	0.17	0.74
S2 (20 m)	16.2 ±22.5	8.3 ±9.4	1.35	0.65	0.50
S2 (40 m)	16.2 ±22.5	17.8 ±23.8	0.30	-0.09	0.82
S2 (80 m)	16.2 ±22.5	29.1 ±32.0	0.96	-0.57	0.32
S4 (5 m)	4.0 ±3.6	4.5 ±4.0	0.18	-0.14	0.71
S4 (10 m)	4.0 ±3.6	4.4 ±3.6	0.07	-0.11	1.00
S4 (20 m)	4.0 ±3.6	5.2 ±4.7	0.50	-0.26	0.43
S4 (40 m)	4.0 ±3.6	6.3 ±5.8	0.60	-0.46	0.57
S4 (80 m)	4.0 ±3.6	18.9 ±12.1	1.46	**-1.30**	**0.0**
S5 (5 m)	25.7 ±40.8	27.1 ±72.8	2.58	-0.05	0.48
S5 (10 m)	25.7 ±40.8	30.1 ±43.0	1.02	-0.16	0.52
S5 (20 m)	25.7 ±40.8	38.5 ±57.9	2.11	-0.40	0.67
S5 (40 m)	25.7 ±40.8	41.1 ±63.8	1.52	-0.48	0.62
S5 (80 m)	25.7 ±40.8	55.6 ±56.2	2.30	**-0.73**	**0.24**
180° approach flow					
S5* (5 m)	42.4 ±131.9	49.4 ±154.7	0.49	-0.15	0.76
S5* (10 m)	42.4 ±131.9	69.8 ±227.2	3.19	-0.49	0.71
S5* (20 m)	42.4 ±131.9	45.9 ±118.8	0.18	-0.08	0.68
S5* (40 m)	42.4 ±131.9	43.8 ±87.2	2.41	-0.03	0.65
S5* (80 m)	42.4 ±131.9	48.3 ±55.9	**7.10**	-0.13	0.50
S6* (5 m)	54.1 ±126.8	57.5 ±127.7	0.21	-0.06	0.78
S6* (10 m)	54.1 ±126.8	58.5 ±155.2	0.47	-0.08	0.89
S6* (20 m)	54.1 ±126.8	59.0 ±136.6	1.32	-0.09	0.78
S6* (40 m)	54.1 ±126.8	53.3 ±94.1	2.91	0.01	0.76
S6* (80 m)	54.1 ±126.8	41.5 ±33.6	**6.19**	0.26	0.54
S7* (5 m)	37.8 ±63.9	37.0 ±70.8	0.39	0.02	0.86
S7* (10 m)	37.8 ±63.9	44.1 ±72.3	0.58	-0.16	0.79
S7* (20 m)	37.8 ±63.9	53.8 ±89.9	1.76	-0.35	0.63
S7* (40 m)	37.8 ±63.9	43.3 ±60.0	2.20	-0.14	0.55
S7* (80 m)	37.8 ±63.9	49.9 ±33.8	1.66	-0.28	0.33
S8* (5 m)	11.4 ±7.8	9.6 ±7.1	0.05	0.18	0.88
S8* (10 m)	11.4 ±7.8	13.5 ±14.1	1.06	-0.16	0.55
S8* (20 m)	11.4 ±7.8	10.6 ±11.2	1.19	0.08	0.42
S8* (40 m)	11.4 ±7.8	31.3 ±40.8	4.06	**-0.93**	0.30
S8* (80 m)	11.4 ±7.8	58.4 ±40.3	1.74	**-1.35**	**0.03**

Table A1. Statistical results of all dispersion simulations performed in the "Michelstadt" wind tunnel simulation study. The cases superscripted with a star were carried out using the reverse approach-flow direction of 180°. Missed acceptance criteria are highlighted in bold font.

source (Δh)	mean wt [ppmv]	mean model [ppmv]	NMSE	FB	FAC2
All (5 m)	32.2 $\pm$80.4	33.0 $\pm$89.5	0.54	-0.02	0.80
All (10 m)	32.2 $\pm$80.4	38.9 $\pm$113.1	1.57	-0.19	0.74
All (20 m)	32.2 $\pm$80.4	38.5 $\pm$89.5	1.72	-0.18	0.61
All (40 m)	32.2 $\pm$80.4	38.3 $\pm$65.4	2.75	-0.17	0.61
All (80 m)	32.2 $\pm$80.4	46.1 $\pm$41.1	3.89	-0.35	0.33
All* (5 m)	37.2 $\pm$91.2	38.5 $\pm$100.2	0.40	-0.03	0.83
All* (10 m)	37.2 $\pm$91.2	46.2 $\pm$129.5	1.48	-0.22	0.75
All* (20 m)	37.2 $\pm$91.2	45.8 $\pm$100.7	1.50	-0.21	0.63
All* (40 m)	37.2 $\pm$91.2	43.2 $\pm$71.2	2.72	-0.15	0.56
All* (80 m)	37.2 $\pm$91.2	49.4 $\pm$40.1	3.97	-0.28	0.35

Table A2. Statistical results derived from the combined data of all simulated sources at the given spatial resolution. The cases superscripted with a star are the combined results of the 180 $^\circ$approach-flow cases only.

References

Appel, K. W., Napelenok, S. L., Foley, K. M., Pye, H. O. T., Hogrefe, C., Luecken, D. J., Bash, J. O., Roselle, S. J., Pleim, J. E., Foroutan, H., Hutzell, W. T., Pouliot, G. A., Sarwar, G., Fahey, K. M., Gantt, B., Gilliam, R. C., Heath, N. K., Kang, D., Mathur, R., Schwede, D. B., Spero, T. L., Wong, D. C., and Young, J. O.: Description and evaluation of the Community Multiscale Air Quality (CMAQ) modeling system version 5.1, Geoscientific Model Development, 10, 1703–1732, doi:10.5194/gmd-10-1703-2017, 2017.

Baik, J.-J., Park, S.-B., and Kim, J.-J.: Urban flow and dispersion simulation using a CFD model coupled to a mesoscale model, Journal of Applied Meteorology and Climatology, 48, 1667–1681, doi:10.1175/2009JAMC2066.1, 2009.

Baumann-Stanzer, K., Andronopoulos, S., Armand, P., Berbekar, E., Efthimiou, G., Fuka, V., Gariazzo, C., Gašparac, G., Harms, F., Hellsten, A., Jurcacova, K., Petrov, A., Rákai, A., Stenzel, S., Tavares, R., Tinarelli, G., and Trini Castelli, S.: COST ES1006 Model evaluation case studies: Approach and results, retrieved from: http://www.elizas.eu/images/Documents/Model%20Evaluation%20Case%20Studies_web.pdf, 2015.

Benavides, J., Snyder, M., Guevara, M., Soret, A., Pérez García-Pando, C., Amato, F., Querol, X., and Jorba, O.: CALIOPE-Urban v1.0: coupling R-LINE with a mesoscale air quality modelling system for urban air quality forecasts over Barcelona city (Spain), Geoscientific Model Development, 12, 2811–2835, doi:10.5194/gmd-12-2811-2019, 2019.

Berbekar, E., Lübcke, M., Harms, F., and Leitl, B.: Validation dataset for local-scale emergency response models, 2013.

Birmili, W., Rehn, J., Vogel, A., Boehlke, C., Weber, K., and Rasch, F.: Micro-scale variability of urban particle number and mass concentrations in Leipzig, Germany, Meteorologische Zeitschrift, 22, 155–165, doi = 10.1127/0941-2948/2013/0394, 2013.

Braess, D.: Towards algebraic multigrid for elliptic problems of second order, Computing, 55, 379–393, doi:10.1007/BF02238488, 1995.

Brandt, A. and Livne, O. E.: Multigrid Techniques, Society for Industrial and Applied Mathematics, doi:10.1137/1.9781611970753, 2011.

Brown, M.: QUIC: A fast, high-resolution 3D building-aware urban transport and dispersion modeling system, AWMA Environmental Manager April issue, pp. 28–31, doi:10.2172/1134791, 2014.

Bröker, O. and Grote, M.: Sparse approximate inverse smoothers for geometric and algebraic multigrid, Applied Numerical Mathematics, 41, 61–80, doi:10.1016/S0168-9274(01)00110-6, 2001.

Calhoun, D. and LeVeque, R. J.: A Cartesian grid finite-volume method for the advection-diffusion equation in irregular geometries, Journal of Computational Physics, 157, 143 – 180, doi:10.1006/jcph.1999.6369, 2000.

Carlino, G., Pallavidino, L., Prandi, R., A., A., Matteucci, G. L., F., R., Bajardi, P., and L., B.: Micro-scale modelling of urban air quality to forecast NO2 critical levels in traffic hot-spots, 2016.

Chang, S. Y.: High Resolution Air Quality Modeling for Improved Characterization of Exposures and Health Risk to Traffic-Related Air Pollutants (TRAPs) in Urban Areas [doctoral-degree thesis], University of North Carolina, Chapel Hill, USA, https://cdr.lib.unc.edu/concern/dissertations/q811kk98b (last access: 08.10.2020), 2016.

Chorin, A.: Numerical solution of the Navier-Stokes equations, Mathematics of Computations, 22, 745–762, doi:10.1090/S0025-5718-1968-0242392-2, 1968.

Croitoru, C. and Nastase, I.: A state of the art regarding urban air quality prediction models, E3S Web of Conferences, 32, 01 010, doi:10.1051/e3sconf/20183201010, 2018.

Deardorff, J. W.: A numerical study of three-dimensional turbulent channel flow at large Reynolds numbers, Journal of Fluid Mechanics, 41, 453–480, doi:10.1017/S0022112070000691, 1970.

Di, P., Xue, J., Hu, C., and Zhou, J.: A cache-efficient parallel Gauss-Seidel solver with alternating tiling, Proceedings of the 15th International Conference on Parallel and Distributed Systems, Shenzhen, 2009, pp. 244–251, doi:10.1109/ICPADS.2009.126, 2009.

Doms, G., Förstner, J., Heise, E., Herzog, H., Mironov, D., Raschendorfer, M., Reinhardt, T., Ritter, B., Schrodin, R., Schulz, J.-P., and Vogel, G.: A description of the nonhydrostatic regional COSMO model. Part II: Physical parameterization. Deutscher Wetterdienst, Offenbach, http://www.cosmo-model.org (last access: 28.12.2020), 2013.

Drew, D.: Mathematical modeling of two-phase flow, Annual Reviews on Fluid Mechanics, 15, 261–291, doi:10.1146/annurev.fl.15.010183.001401, 1983.

Efstathiou, G. A., Beare, R. J., Osborne, S., and Lock, A. P.: Grey zone simulations of the morning convective boundary layer development, Journal of Geophysical Research: Atmospheres, 121, 4769–4782, doi:10.1002/2016JD024860, 2016.

Fallah-Shorshani, M., Shekarrizfard, M., and Hatzopoulou, M.: Integrating a street-canyon model with a regional Gaussian dispersion model for improved characterisation of near-road air pollution, Atmospheric Environment, 153, 21–31, doi:10.1016/j.atmosenv.2017.01.006, 2017.

Fernández, G., Rezzano Tizze, N., D'Angelo, M., and Mendina, M.: Numerical simulation of different pollution sources in an urban environment, E3S Web of Conferences, 128, 10 005, doi:10.1051/e3sconf/201912810005, 2019.

Flemming, J., Huijnen, V., Arteta, J., Bechtold, P., Beljaars, A., Blechschmidt, A.-M., Diamantakis, M., Engelen, R. J., Gaudel, A., Inness, A., Jones, L., Josse, B., Katragkou, E., Marecal, V., Peuch, V.-H., Richter, A., Schultz, M. G., Stein, O., and Tsikerdekis, A.: Tropospheric chemistry in the Integrated Forecasting System of ECMWF, Geoscientific Model Development, 8, 975–1003, doi:10.5194/gmd-8-975-2015, 2015.

Grell, G. A., Peckham, S. E., Schmitz, R., McKeen, S. A., Frost, G., Skamarock, W. C., and Eder, B.: Fully coupled “online” chemistry within the WRF model, Atmospheric Environment, 39, 6957–6975, doi:10.1016/j.atmosenv.2005.04.027, 2005.

Haga, C. J. B.: Numerical methods for basin-scale poroelastic modelling [doctoral-degree thesis], University of Oslo, Oslo, Norway, http://urn.nb.no/URN:NBN:no-29117 (last access: 08.10.2020), 2011.

Hanna, S. and Chang, J.: Acceptance criteria for urban dispersion model evaluation, Meteorology and Atmospheric Physics, 116, 133–146, doi:10.1007/s00703-011-0177-1, 2012.

Hanna, S. R., Brown, M. J., Camelli, F. E., Chan, S. T., Coirier, W. J., Hansen, O. R., Huber, A. H., Kim, S., and Reynolds, R. M.: Detailed simulations of atmospheric flow and dispersion in urban downtown areas by computational fluid dynamics (CFD) models - an application of five CFD models to Manhattan, Bulletin of the American Meteorological Society, 87, 1713–1726, doi:10.1175/BAMS-87-12-1713, 2006.

Harrison, R.: Urban atmospheric chemistry: a very special case for study, npj Climate and Atmospheric Science, 1, 20 175–20 180, doi:10.1038/s41612-017-0010-8, 2018.

Haupt, S. E., Kosovic, B., Shaw, W., Berg, L. K., Churchfield, M., Cline, J., Draxl, C., Ennis, B., Koo, E., Kotamarthi, R., Mazzaro, L., Mirocha, J., Moriarty, P., Muñoz-Esparza, D., Quon, E., Rai, R. K., Robinson, M., and Sever, G.: On bridging a modeling scale gap: Mesoscale to microscale coupling for wind energy, Bulletin of the American Meteorological Society, 100, 2533–2550, doi:10.1175/BAMS-D-18-0033.1, 2019.

Hicken, J., Ham, F., Militzer, J., and Koksal, M.: A shift transformation for fully conservative methods: turbulence simulation on complex, unstructured grids, Journal of Computational Physics, 208, 704 – 734, doi:10.1016/j.jcp.2005.03.002, 2005.

Jensen, S. S., Ketzel, M., Becker, T., Christensen, J., Brandt, J., Plejdrup, M., Winther, M., Nielsen, O.-K., Hertel, O., and Ellermann, T.: High resolution multi-scale air quality modelling for all streets in Denmark, Transportation Research Part D: Transport and Environment, 52, 322 – 339, doi:10.1016/j.trd.2017.02.019, 2017.

Jähn, M., Knoth, O., König, M., and Vogelsberg, U.: ASAM v2.7: A compressible atmospheric model with a Cartesian cut cell approach, Geoscientific Model Development, 8, 317–340, doi:10.5194/gmd-8-317-2015, 2015.

Kadaverugu, R., Sharma, A., Matli, C., and Biniwale, R.: High resolution urban air quality modeling by coupling CFD and mesoscale models: a review, Asia-Pacific Journal of Atmospheric Sciences, 55, 539–556, doi:10.1007/s13143-019-00110-3, 2019.

Kanda, M., Inagaki, A., Miyamoto, T., Gryschka, M., and Raasch, S.: A new aerodynamic parametrization for real urban surfaces, Boundary-Layer Meteorology, 148, 357–377, doi:10.1007/s10546-013-9818-x, 2013.

Karam, M., Sutherland, J., Hansen, M., and Saad, T.: A Framework for Analyzing the Temporal Accuracy of Pressure Projection Methods, AIAA Aviation 2019 Forum, doi:10.2514/6.2019-3634, 2019.

Kemm, F., Gaburro, E., Thein, F., and Dumbser, M.: A simple diffuse interface approach for compressible flows around moving solids of arbitrary shape based on a reduced Baer-Nunziato model, Computers Fluids, 204, 104 536–104 561, doi:10.1016/j.compfluid.2020.104536, 2020.

Kim, Y., Sartelet, K., Raut, J.-C., and Chazette, P.: Influence of an urban canopy model and PBL schemes on vertical mixing for air quality modeling over Greater Paris, Atmospheric Environment, 107, 289 – 306, doi:https://doi.org/10.1016/j.atmosenv.2015.02.011, 2015.

Korhonen, A., Lehtomäki, H., Rumrich, I., Karvosenoja, N., Paunu, V., Kupiainen, K., Sofiev, M., Palamarchuk, Y., Kukkonen, J., Kangas, L., Karppinen, A., and Hänninen, O.: Influence of spatial resolution on population PM2.5 exposure and health impacts, Air Quality, Atmosphere Health, 12, 705–718, doi:10.1007/s11869-019-00690-z, 2019.

Kurppa, M., Roldin, P., Strömberg, J., Balling, A., Karttunen, S., Kuuluvainen, H., Niemi, J. V., Pirjola, L., Rönkkö, T., Timonen, H., Hellsten, A., and Järvi, L.: Sensitivity of spatial aerosol particle distributions to the boundary conditions in the PALM model system 6.0, Geoscientific Model Development Discussions, 2020, 1–33, doi:10.5194/gmd-2020-163, 2020.

Larsson, J., Lien, F. S., and Yee, E.: Conditional semicoarsening multigrid algorithm for the Poisson equation on anisotropic grids, Journal of Computational Physics, 208, 368–383, doi:10.1016/j.jcp.2005.02.020, 2005.

Lee, M., Leitl, B., and Patnaik, G.: Model and application-specific validation data for LES-based transport and diffusion models, Proceedings of the Eighth Conference on Coastal Atmospheric and Oceanic Prediction and Processes, Phoenix, Arizona, 2009.

Llorente, I. M. and Melson, N. D.: Behavior of plane relaxation methods as multigrid smoothers, Electronic Transactions on Numerical Analysis, 10, 92–114, 2000.

Louis, J. A.: A parametric model of vertical eddy fluxes in the atmosphere, Boundary-Layer Meteorology, 17, 187–202, doi:10.1007/BF00117978, 1979.

Maronga, B., Gross, G., Raasch, S., Banzhaf, S., Forkel, R., Heldens, W., Kanani-Sühring, F., Matzarakis, A., Mauder, M., Pavlik, D., Pfafferott, J., Schubert, S., Seckmeyer, G., Sieker, H., and Winderlich, K.: Development of a new urban climate model based on the model PALM–Project overview, planned work, and first achievements, Meteorologische Zeitschrift, 28, 105–119, doi:10.1127/metz/2019/0909, 2019.

Martilli, A., Clappier, A., and Rotach, M.: An urban surface exchange parameterisation for mesoscale models, Boundary-Layer Meteorology, 104, 261–304, doi:10.1023/A:1016099921195, 2002.

Miller, M. J. and Thorpe, A. J.: Radiation conditions for the lateral boundaries of limited-area numerical models, Quarterly Journal of the Royal Meteorological Society, 107, 615–628, doi:10.1002/qj.49710745310, 1981.

Mittal, R. and Iaccarino, G.: Immersed boundary methods, Annual Review of Fluid Mechanics, 37, 239–261, doi:10.1146/annurev.fluid.37.061903.175743, 2005.

Mohr, M. and Wienands, R.: Cell-centred multigrid revisited, Computing and Visualization in Science, 7, 129–140, doi:10.1007/S00791-004-0137-0, 2004.

Noh, Y., C. W. H. S. and Raasch, S.: Improvement of the K-profile Model for the Planetary Boundary Layer based on Large Eddy Simulation Data, Boundary-Layer Meteorology, 107, 401–427, doi:10.1023/A:1022146015946, 2003.

Paas, B., Schmidt, T., Markova, S., Maras, I., Ziefle, M., and Schneider, C.: Small-scale variability of particulate matter and perception of air quality in an inner-city recreational area in Aachen, Germany, Meteorologische Zeitschrift, 25, 305–317, doi:10.1127/metz/2016/0704, 2016.

Rakai, A. and Gergely, K.: Microscale obstacle resolving air quality model evaluation with the Michelstadt case, The Scientific World Journal, 2013, 781 748, doi:10.1155/2013/781748, 2013.

Rieger, D., Bangert, M., Bischoff-Gauss, I., Förstner, J., Lundgren, K., Reinert, D., Schröter, J., Vogel, H., Zängl, G., Ruhnke, R., and Vogel, B.: ICON–ART 1.0 – a new online-coupled model system from the global to regional scale, Geoscientific Model Development, 8, 1659–1676, doi:10.5194/gmd-8-1659-2015, 2015.

Schatzmann, M., Leitl, B., Harms, F., and Hertwig, D.: Field data versus wind tunnel data: The art of validating urban flow and dispersion models, Proceedings of the 9th Asia-Pacific Conference on Wind Energy, Auckland, New Zealand, doi:10.17608/k6.auckland.5630923.v1, 2017.

Schubert, S., Grossman-Clarke, S., and Martilli, A.: A double-canyon radiation scheme for multi-layer urban canopy models, Boundary-Layer Meteorology, 145, 439–468, doi:10.1007/s10546-012-9728-3, 2012.

Schumann, U.: Subgrid scale model for finite difference simulations of turbulent flows in plane channels and annuli, Journal of Computational Physics, 18, 376 – 404, doi:10.1016/0021-9991(75)90093-5, 1975.

Sedlacek, M.: Sparse approximate inverses for preconditioning, smoothing, and regularization [doctoral-degree thesis], Technical University of Munich, Munich, Germany, https://d-nb.info/1029819246/34 (last access: 08.10.2020), 2012.

Shu, C.-W.: Essentially non-oscillatory and weighted essentially non-oscillatory schemes for hyperbolic conservation laws, Lecture Notes in Mathematics, Springer, Berlin, Heidelberg, 1998.

Stull, R. B.: An Introduction to Boundary Layer Meteorology, 1988.

Sweby, P. K.: High Resolution Schemes Using Flux Limiters for Hyperbolic Conservation Laws, SIAM Journal on Numerical Analysis, 21, 995–1011, doi:10.2307/2156939, 1984.

Tang, W.-p. and Wan, J.: Sparse approximate inverse smoother for multigrid, SIAM Journal on Matrix Analysis and Applications, 21, doi:10.1137/S0895479899339342, 2000.

Wang, J., Mao, J., Zhang, Y., Cheng, T., Yu, Q., Tan, J., and Ma, W.: Simulating the effects of urban parameterizations on the passage of a cold front during a pollution episode in megacity Shanghai, Atmosphere, 10, 79, doi:10.3390/atmos10020079, 2019.

Wicker, L. J. and Skamarock, W. C.: A time-splitting scheme for the elastic equations incorporating second-order Runge–Kutta time differencing, Monthly Weather Review, 126, 1992–1999, doi:10.1175/1520-0493(1998)126<1992:ATSSFT>2.0.CO;2, 1998.

Wolf, T., Pettersson, L. H., and Esau, I.: A very high-resolution assessment and modelling of urban air quality, Atmospheric Chemistry and Physics, 20, 625–647, doi:10.5194/acp-20-625-2020, 2020.

Wolke, R., Knoth, O., Hellmuth, O., Schröder, W., and Renner, E.: The parallel model system LM-MUSCAT for chemistry-transport simulations: Coupling scheme, parallelization and applications, 13, 363 – 369, doi:10.1016/S0927-5452(04)80048-0, 2004.

Wolke, R., Schröder, W., Schrödner, R., and Renner, E.: Influence of grid resolution and meteorological forcing on simulated European air quality: A sensitivity study with the modeling system COSMO-MUSCAT, Atmospheric Environment, 53, 110 – 130, doi:doi.org/10.1016/j.atmosenv.2012.02.085, 2012.

Wu, X.: Inflow turbulence generation methods, Annual Review of Fluid Mechanics, 49, 23–49, doi:10.1146/annurev-fluid-010816-060322, 2017.

Xie, Z. and Castro, I. P.: LES and RANS for turbulent flow over arrays of wall-mounted obstacles, Flow, Turbulence and Combustion, 76, 291, doi:doi.org/10.1007/s10494-006-9018-6, 2006.

Yang, X., Park, G., and Moin, P.: Log-layer mismatch and modeling of the fluctuating wall stress in wall-modeled large-eddy simulations, Physical Review Fluids, 2, doi:10.1103/PhysRevFluids.2.104601, 2017.

Yavneh, I.: On Red-Black SOR Smoothing in Multigrid, SIAM Journal on Scientific Computing, 17, 180–192, doi:10.1137/0917013, 1996.